Xu, Ming H.; Savolainen, Tuomas; Zubko, Nataliya; Poutanen, Markku; Lunz, Susanne; Schuh, Harald; Wang, Guang L.

Imaging VGOS Observations and Investigating Source Structure Effects

Published in:
Journal of Geophysical Research: Solid Earth

DOI:
10.1029/2020JB021238

Published: 01/04/2021

Document Version
Publisher's PDF, also known as Version of record

JGR Solid Earth

RESEARCH ARTICLE
10.1029/2020JB021238

Imaging VGOS Observations and Investigating Source Structure Effects

Ming H. Xu[1,2,6,7], Tuomas Savolainen[1,2,3], Nataliya Zubko[4], Markku Poutanen[4], Susanne Lunz[5], Harald Schuh[6,5], and Guang L. Wang[7]

[1]Aalto University Metsähovi Radio Observatory, Kylmälä, Finland, [2]Aalto University Department of Electronics and Nanoengineering, Aalto, Finland, [3]Max-Planck-Institut für Radioastronomie, Bonn, Germany, [4]Finnish Geospatial Research Institute, Masala, Finland, [5]Deutsches GeoForschungsZentrum (GFZ), Potsdam, Germany, [6]Institute of Geodesy and Geoinformation Science, Technische Universität Berlin, Berlin, Germany, [7]Shanghai Astronomical Observatory, Chinese Academy of Sciences, Shanghai, P.R. China

Key Points:

- Images of radio sources at the four bands were derived directly from VGOS broadband observations
- Source structure effects in VGOS observations were modeled and verified
- The alignments of the images at the various frequency bands were revealed to be very important in correcting source structure effects in VGOS observations

Correspondence to:
M. H. Xu,
minghui.xu@aalto.fi

Citation:
Xu, M. H., Savolainen, T., Zubko, N., Poutanen, M., Lunz, S., Schuh, H., & Wang, G. L. (2021). Imaging VGOS observations and investigating source structure effects. *Journal of Geophysical Research: Solid Earth*, *126*, e2020JB021238. https://doi.org/10.1029/2020JB021238

Received 23 OCT 2020
Accepted 12 MAR 2021

Abstract The next-generation, broadband geodetic very long baseline interferometry system, named VGOS, is being developed globally with an aim to achieve 1 mm accuracy for station positions. Currently, the systematic errors in VGOS broadband delays are still about 20 ps. In this study, we demonstrate that it is feasible to make images directly from VGOS observations without the need of complicated calibrations and determine the source structure effects in VGOS broadband delays through the process of model fitting to the structure phases from our imaging results. Source structure effects are investigated in detail, and it is shown that the systematic errors in VGOS observations are well explained by these effects. For instance, the root-mean-square (RMS) closure delays of the observations of sources 0016 + 731 and 1030 + 415 are 24.9 and 50.2 ps in session VO0034, respectively; after correcting source structure effects based on the images, the RMS values of the residual closure delays are 5.5 and 10.1 ps. The jumps in delay observables with magnitudes of several hundreds of picoseconds are found to be caused by 2π phase shifts among the four bands due to strong source structure effects. The impact of the alignment of the images at the four frequency bands in VGOS is discussed. Our study provides a methodology for deriving images of radio sources at the four bands of VGOS observations and discusses the alignment of the images at the four bands, which is fundamental to mitigating these systematic effects.

1. Introduction

Geodetic very long baseline interferometry (VLBI) is a space-geodetic technique that has regularly made global astrometric/geodetic observations since 1979, which are the basis for creating the International Celestial Reference Frame (ICRF2; Fey et al., 2015) and obtaining a full set of Earth Orientation Parameters. Together with other three space-geodetic techniques, that is, Global Navigation Satellite Systems (GNSS), Satellite Laser Ranging (SLR), and Doppler Orbitography and Radiopositioning Integrated by Satellite (DORIS), VLBI plays an important role in establishing the International Terrestrial Reference Frame (ITRF; Altamimi et al., 2016). Requirements for the ITRF have increased dramatically since the 1980s, and the most stringent one from sea level studies is 1 mm position accuracy and 0.1 mm/yr velocity stability on global scales.

The International VLBI Service for Geodesy and Astrometry (IVS; Nothnagel et al., 2017; Schuh & Behrend, 2012; please see https://ivscc.gsfc.nasa.gov/index.html) is developing the next-generation geodetic VLBI system, known as the VLBI Global Observing System (VGOS; Niell et al., 2007; Petrachenko et al., 2009) in order to achieve the goal of 1 mm accuracy. This is one order of magnitude beyond the capability of the traditional S/X VLBI system. Although the VGOS observations from the 500-km-long baseline, GGAO12M-WESTFORD, have obtained geodetic results of a weighted root-mean-square deviation of the baseline length residuals about the weighted mean of 1.6 mm (Niell et al., 2018), few studies have analyzed error sources in the VGOS observations, for instance source structure effects, to evaluate the capability of this new VLBI system. Source structure effects hardly have any influence on this short baseline but can cause significant errors in observations of longer baselines, as demonstrated by the residual delays from geodetic solutions of VGOS observations in Bolotin et al. (2019). Celestial radio sources observed by geodetic VLBI, mostly quasars, are treated as point-like sources in routine geodetic solutions, but in fact they are

resolved on intercontinental baselines. The questions are how large is their effect on the reference frames and how can these effects be corrected or/and mitigated.

The dominant remaining error source in traditional S/X observations was shown to be source structure effects based on analyzing closure delays (Anderson & Xu, 2018; Xu et al., 2016, 2017), and source structure is one of the primary factors causing source position differences between the radio and optical catalogs (Xu et al., 2021). A study of 21 VGOS sessions revealed that the random measurement noise of VGOS group delays was about two picoseconds (ps), while the contributions from systematic error sources were at the level of 20 ps (Xu et al., 2020). Discrete jumps in VGOS delays with magnitudes of several hundreds of picoseconds or even larger have been reported. These systematic error sources were considered to be related to source structure effects, the in-depth investigation of which would require images of radio sources at the wide frequency range of VGOS observations. It is not possible for VGOS to achieve its goal without taking source structure effects into account, since they are so overwhelming in VGOS observations, even for the sources with minimum structure (Xu et al., 2020). In this study, we attempt to investigate these systematic errors by making images directly from VGOS observations and modeling structure effects from the imaging results.

The study is structured as follows. In Section 2, we introduce the data and the imaging process, perform imaging simulations and determine structure effects in broadband observations. In Section 3, we describe the comparison of modeled structure effects and the systematic effects in observations and study the impact of source structure effects. The discussion of the reference points of the images is presented in Section 4; the so-called core shift, leading to complexity in the alignment of the images at different frequencies, is also discussed. Conclusions are made in Section 5.

2. Data and Methodology

2.1. VGOS Observations

VGOS observations mainly rely on the advantages from the small (~12 m in diameter) and fast slewing radio telescopes, ultrawideband receivers (from 2 to 14 GHz), and the expectation of continuous operation, 24 h a day and 7 days a week. Currently, they are made simultaneously at four 512-MHz bands centered at 3.3, 5.5, 6.6, and 10.5 GHz with 32 recording channels (eight channels per band; see the detailed technical description of the observing frequency setup in Niell et al., 2018). On rare occasions there are 31 channels recorded. For instance, in session VO0034 station ONSA13SW recorded with 31 channels with one missing at the highest frequency band. However, we will always refer to as channels in the paper for simplicity. Group delay, phase at the reference frequency, and phase dispersion, which is primarily due to differential total electron content (δTEC) along the line of sight through the ionosphere, are estimated simultaneously from the four-band observations in the VGOS data processing (Cappallo, 2014). The group delay, the phase at 6 GHz, and the δTEC are referred to as broadband observables. The reported formal errors of the group delay observables in databases are just a few picoseconds (ps), and those of the δTEC observables are at the level smaller than 0.1 TECU (1 TECU $\equiv 10^{16}$ electrons per square meter). Based on closure analysis in Xu et al. (2020), as mentioned earlier, the random measurement noise level of VGOS group delays was confirmed to be 2 ps by combining the VGOS observations from the radio sources that have log closure amplitude root-mean-square values smaller than 0.25 (Xu et al., 2019), and the contributions from other systematic error sources were at the level of 20 ps.

Thirty-four IVS VGOS sessions are publicly available as of June 2020. However, the study reported here concentrates on two sessions VT9217 and VO0034 (observed on August 5, 2019 and February 3, 2020, respectively) to investigate source structure effects in VGOS in detail and to discuss the difficulties in this process in a concrete manner. A complete investigation into the correction of source structure effects in geodetic VLBI solutions for all the VGOS observations available is in preparation. Session VO0034 utilized the most stations among these 34 sessions, and thus has the best (u, v) coverage critical for imaging. Session VT9217 was selected without preference. The locations of the VGOS stations in these two sessions are shown in Figure 1.

VGOS observations in the vgosDB format (Gipson, 2012) based on the NetCDF library were used to generate the corresponding uvfits data. The correlated amplitudes at the 32 channels, written in the NetCDF file

Figure 1. Locations of the VGOS stations in session VT9217 (red pluses) and session VO0034 (blue circles). The two stations ONSA13NE and ONSA13SW are located at the same site. VGOS, VLBI Global Observing System.

ChannelInfo_bX.nc with a variable name of "ChanAmpPhase," were averaged at each of the four bands to assign the amplitude observables, and the formal errors of the mean amplitudes based on the standard deviations were used as their uncertainties. The structure differences across the 512 MHz bandwidth of each of the four bands were ignored in this study. (Indeed, this assumption may not hold for some sources. In such cases, the derived uncertainty of the averaged amplitude indicates the changing structure within each band rather than its accuracy.) Based on the uncertainties of amplitudes, the signal-to-noise ratios (SNR) were determined and then used to define the uncertainties of the phase observables. Through investigations of phase observables in the vgosDB data set, it is evident that the phases of the 32 channels stored in the same file with the same variable name as channel amplitude observables are actually residual phases after model fitting rather than the total phases that we needed. Therefore, three types of VGOS observables, namely residual phases, geocentric group delays (note that geocentric group delay refers to baseline group delay with a timestamp referring the geocenter), and δTEC estimates, were combined to recover the observed total phases at each of the four bands. The uncertainties of these phase observables were based on the previously derived SNRs from the observed amplitudes.

In the VGOS data processing (see ftp://ivs.bkg.bund.de/pub/vgos_corr_workshop/vgos-data-processing.pdf for the VGOS data processing manual), all 128 correlation products (four polarization products at each channel, eight channels per band, and four bands) are combined to give a single pseudo-Stokes *I* observable, taking into account the differential parallactic angles between stations (Cappallo, 2016). Pseudo-Stokes *I*, however, does not take the gain differences between various polarizations or leakage into account. This leads to systematic, nonclosing errors in the resulting closure quantities, which depend on the polarizations of radio sources, feed purity, and gain differences between the horizontal and vertical polarizations in a complex manner. So far we ignore these issues and assign the amplitudes and phases as Stokes *I* coefficients. Thus, there is one amplitude and one residual phase for each of the 32-MHz channels; in other words, eight per band of each.

For completeness, we give the basic equations that were used to generate the imaging data. The amplitude *V* at each of the four bands is given as the mean of the channel amplitudes, as follows:

$$\mathbf{V} = \frac{\sum_{i=1}^{\mathbf{L}} \mathbf{V_i}}{\mathbf{L}}, \tag{1}$$

where V_i is the visibility amplitude in the *i*th channel of the band and L is the number of validated channels with a maximum value of 8. The phase ϕ of the band with the central frequency $\bar{\nu}$ is reconstructed from

the values of the channel residual phases, the group delay, and the δTEC observable of each observation, as follows:

$$\phi = \frac{\sum_{i=1}^{L} \Delta\phi_i}{L} + \tau(\bar{\nu} - \nu_0) - \frac{k\,\delta\mathrm{TEC}}{\bar{\nu}}, \tag{2}$$

where $\Delta\phi_i$ is the residual phase in the ith channel of the band, τ and δTEC are the broadband delay and the differential total electron content from the observation, ν_0 is the reference frequency of 6.0 GHz, and k is a constant. $k = 1.3445$ when phases are in units of a turn of a cycle, delays in units of nanosecond, frequencies in units of GHz, and δTEC in units of TECU.

In this study, the uncertainty of amplitude $\sigma(V)$ is statistically determined as the formal error of the mean amplitude for each band by

$$\sigma(V) = \sqrt{\frac{\sum_{i=1}^{L}(V_i - V)^2}{L(L-1)}}. \tag{3}$$

With the amplitude V and its uncertainty $\sigma(V)$, the SNR is actually defined. The uncertainty of phase $\sigma(\phi)$ is so defined that it complies with the SNR defined by the corresponding amplitude observable.

For a triangle of three stations, a, b, and c, closure phase is defined by

$$\phi_{\mathrm{clr}} = \phi_{ab} + \phi_{bc} + \phi_{ca}, \tag{4}$$

where, for instance, ϕ_{ab} is the geocentric phase observable on baseline ab. The closure phase uncertainty, $\sigma(\phi_{\mathrm{clr}})$, is derived from the uncertainties of phase observables on the three baselines. With a network of M stations, there are at most $M(M-1)(M-2)/6$ closure phases available with a subset of $(M-1)(M-2)/2$ independent with each other.

With one more station d, log closure amplitude V_{clr} is defined as

$$V_{\mathrm{clr}} = V_{abcd} = \ln\left(\frac{V_{ab}V_{cd}}{V_{ac}V_{bd}}\right), \tag{5}$$

where for instance, V_{ab} is the amplitude observable on baseline ab. Note that the sequence of the four stations in a closure amplitude is relevant; with the same four stations, three closure amplitudes with different magnitudes can be formed. The uncertainty of log closure amplitude $\sigma(V\mathrm{clr})$, for example for V_{abcd}, is determined by

$$\sigma(V_{\mathrm{clr}}) = \sigma(V_{abcd}) = \sqrt{\left(\frac{\sigma(V_{ab})}{V_{ab}}\right)^2 + \left(\frac{\sigma(V_{cd})}{V_{cd}}\right)^2 + \left(\frac{\sigma(V_{ac})}{V_{ac}}\right)^2 + \left(\frac{\sigma(V_{bd})}{V_{bd}}\right)^2}, \tag{6}$$

where for instance, $\sigma(V_{ab})$ is the uncertainty of the amplitude on baseline ab as defined by Equation 3. There are at most $M(M-1)(M-2)(M-3)/8$ closure amplitudes with only $M(M-3)/2$ independent ones among them.

Since the full set of closure phases—as well as closure amplitudes—is not independent, a complete noise covariance needs to be taken into account in the imaging process when the full set of closure quantities is used (Blackburn et al., 2020). In this study, we selected a subset of independent closure quantities to be used. Geodetic VLBI observations generally have high enough SNR, so we flagged the observations with total SNR from the combination of the 128 correlation products lower than 25 to get rid of a small fraction of low SNR observations.

2.2. Imaging VGOS Observations

The standard algorithm for astrophysical interferometric imaging is CLEAN (Clark, 1980; Högbom, 1974). It decomposes a dirty image obtained from an inverse Fourier transform of the sparely sampled visibilities into multiple point sources and usually iterates the calibration and CLEAN processes using the information of the image obtained from the previous step, so-called "self-calibration" or "hybrid-mapping" (e.g., Cornwell & Wilkinson, 1981; Pearson & Readhead, 1984; Thompson et al., 2017; Wilkinson et al., 1977). In addition to the CLEAN algorithm, another commonly used interferometric imaging approach, named regularized maximum likelihood (RML), solves for the pixels' fluxes in a source image by fitting directly to the data. RML applies regularization and constraints, such as entropy, sparsity, or smoothness, to solve the ill-posed problem in this imaging process (e.g., Narayan & Nityananda, 1986; Nityananda & Narayan, 1983). It is more flexible for the RML algorithm to use different data terms than the standard CLEAN algorithm, for instance, visibility phases, visibility amplitudes, closure phases, (log) closure amplitudes or various combinations of them. In the analysis presented here, we used the RML approach to make images by fitting directly closure phases and *log* closure amplitudes from VGOS observations. We thus can simplify the interferometric calibration process because most calibration errors can be treated as station-based gain errors (e.g., Hamaker et al., 1996; Thompson et al., 2017) and thus are canceled out in closure phases and closure amplitudes. Meanwhile, in addition to corrections of the phase calibration systems, in the VGOS data processing additional channel-to-channel phase corrections were applied to various polarization products, but they are station-based as well. These are the reasons for using the RML imaging method to derive images from closure phases and amplitudes for VGOS observations. The eht-imaging library (ehtim; Chael et al., 2016, 2018, see https://github.com/achael/eht-imaging for its documentation) was used to make images from the data that we generated from VGOS observations. This library constructs an objective function based on the user-specified data terms, regularizer terms, and hyperparameters and progresses toward a minimum in the objective function by using the limited-memory BFGS algorithm (Byrd et al., 1995). The ehtim library has been extensively tested for making images from closure quantities (Chael et al., 2016, 2018), and it was successfully used in making of the seminal image of the black hole shadow in galaxy M87 by Event Horizon Telescope Collaboration et al. (2019).

An automated python script was developed to use the ehtim library based on the objective functions and iteration processes that were tested to be suitable for VGOS observations. The field of view (FOV) was 6.0 × 6.0 milliarcseconds (mas) with 600 × 600 pixels, which allows the positions of structure components to be defined in the images themselves with an accuracy better than 10 microarcseconds (μas). In principle, both FOV and pixel dimensions can be increased. If the FOV increased, however, it would be time-consuming in both the imaging process and the structure-phase calculations from the images to keep the pixel spacing at 10 μas. As long as the beam sizes fitted from actual observations are significantly smaller than this FOV, it is appropriate for the images of nearly all VGOS radio sources, which are selected to have compact structure.

In our RML imaging, we used the isotropic total variation regularization, which applies a smoothness constraint to the derived image and has been shown to be effective to obtain superresolution images, about a quarter of the diffraction limit, from visibility amplitudes and closure phases (e.g., Akiyama et al., 2017); the weighting of closure phases and closure amplitudes were set to be the numbers of independent closure phases and closure amplitudes for each source. We broke the whole iteration process into several rounds with 30 or 70 iterations each. We started with a point source. Later on, within each round the image from the previous fitting was taken as a priori, while it was convolved with a Gaussian of the size of half of the beam size to produce the a priori model in transition to the next round. This process can help in avoiding a local minimum of the objective function. The final images, obtained directly from fitting without convolving, are super-resolved compared to the nominal beam size, but it has been shown that the RML method is capable of such superresolution (Chael et al., 2016). This procedure was applied to derive images for all radio sources.

The direct equivalence of making images based on closure quantities and self-calibration of complex visibilities was demonstrated by Blackburn et al. (2020) in both analytical and numerical ways. However, the image derived solely from closure quantities does not have the correct flux scaling, which is fortunately not important to model the effects of source structure in geodetic VLBI observables. It is possible to register the

total flux densities for closure images when the system equivalent flux density measurements are available for more than two stations; this is under investigation.

2.3. Imaging Simulations and Evaluations

To test this imaging process and evaluate the image fidelity, we simulated VLBI observations based on the superresolution images of six sources, as listed in Table 1, from the Monitoring Of Jets in Active galactic nuclei with VLBA Experiments (MOJAVE; Lister et al., 2018). These MOJAVE images were used as the ground truth models to evaluate the reconstructed images from the simulated data.

The simulated data were generated by assuming that they were produced by the same stations at the same epochs as the actual observations of a given source in session VO0034, but observed at the frequency of 15.3 GHz. One data set was produced for each individual source in that session, and we did it for all the 80 radio sources one by one. As stated previously, closure quantities are insensitive to station-based errors, and it is shown by Chael et al. (2018) that closure-based images from the data with arbitrary levels of station-based gain errors are consistent with the tested model. It is thus only important to consider baseline-dependent errors; noise was added for each simulated observation to produce the same SNR as the actual observation in VO0034. We then reconstructed an image based on closure amplitudes and closure phases from each of the simulated data sets by applying the procedure described in the previous section. To quantitatively evaluate the fidelity of the derived images from these simulated data, we adopted the so-called normalized root-mean-square error (NRMSE) (Chael et al., 2018), which is a pixel-to-pixel metric and is defined as follows:

$$\mathrm{NRMSE} = \frac{\sqrt{\sum_{i=1}^{J}(A_i - B_i)^2}}{\sqrt{\sum_{i=1}^{J}(B_i)^2}}, \tag{7}$$

where A_i and B_i are the flux of the ith pixel in image A under investigation and image B as the model, both with J pixels in total. Before computing NRMSE, both the model image and the reconstructed image were blurred with one fifth of the beam size fitted from the simulated data to have the same angular resolution and were aligned by searching for the maximum cross correlation between them. The simulations in Chael et al. (2018) showed that the NRMSE with a value of ~0.2 or smaller indicates an image consistent with the model.

The results for the MOJAVE image of source 0642 + 449 as the ground truth model are shown in Figure 2. The model image is shown in the top-left corner. It has a typical structure of the geodetic VLBI sources, with a core and a jet separated by a few hundred microarcseconds (μas). Thirty reconstructed images from the simulated data set follow in the bottom. (Among the 80 sources in VO0034, the observations of 35 sources have formed closure phases and closure amplitudes and thus have been imaged. Due to the page limit, the images for the five sources with the least observations were not shown.) In the figure, they are sorted in the decreasing order of the number of scans with more than four stations in session VO0034. As a function of these scan numbers, the calculated NRMSE values of these images are shown in the top right corner as well as the maximum cross-correlation values. With the simulated data set equivalent to each of the 18 radio sources that were observed with more than 20 such scans, the reconstructed images have NRMSE values smaller than 0.15 and maximum cross correlations larger than 0.99. These 18 images are consistent with the model. With fewer scans, however, the NRMSE values increased significantly to ~0.6. With the number of scans in the range of 10–20, it is still possible to derive a reasonably good image. Similar conclusion can be made based on the simulations of the other five MOJAVE sources. These simulations preliminarily set the minimum number of scans in a 24-h session to be 10–12 in order to make images with good fidelity, given a blind scheduling in the sense of the imaging (u, v) coverage and a similar VGOS network as in these VGOS sessions.

A series of further tests were done to investigate the impact of outliers on the imaging results. For each set of the previously simulated data, one observation in the scan with more than six stations observing was changed by shifting its phase by 50° and its amplitude by 200%. We then produced images from these revised data. The simulations revealed that the imaging results were not significantly affected by that outlier for the

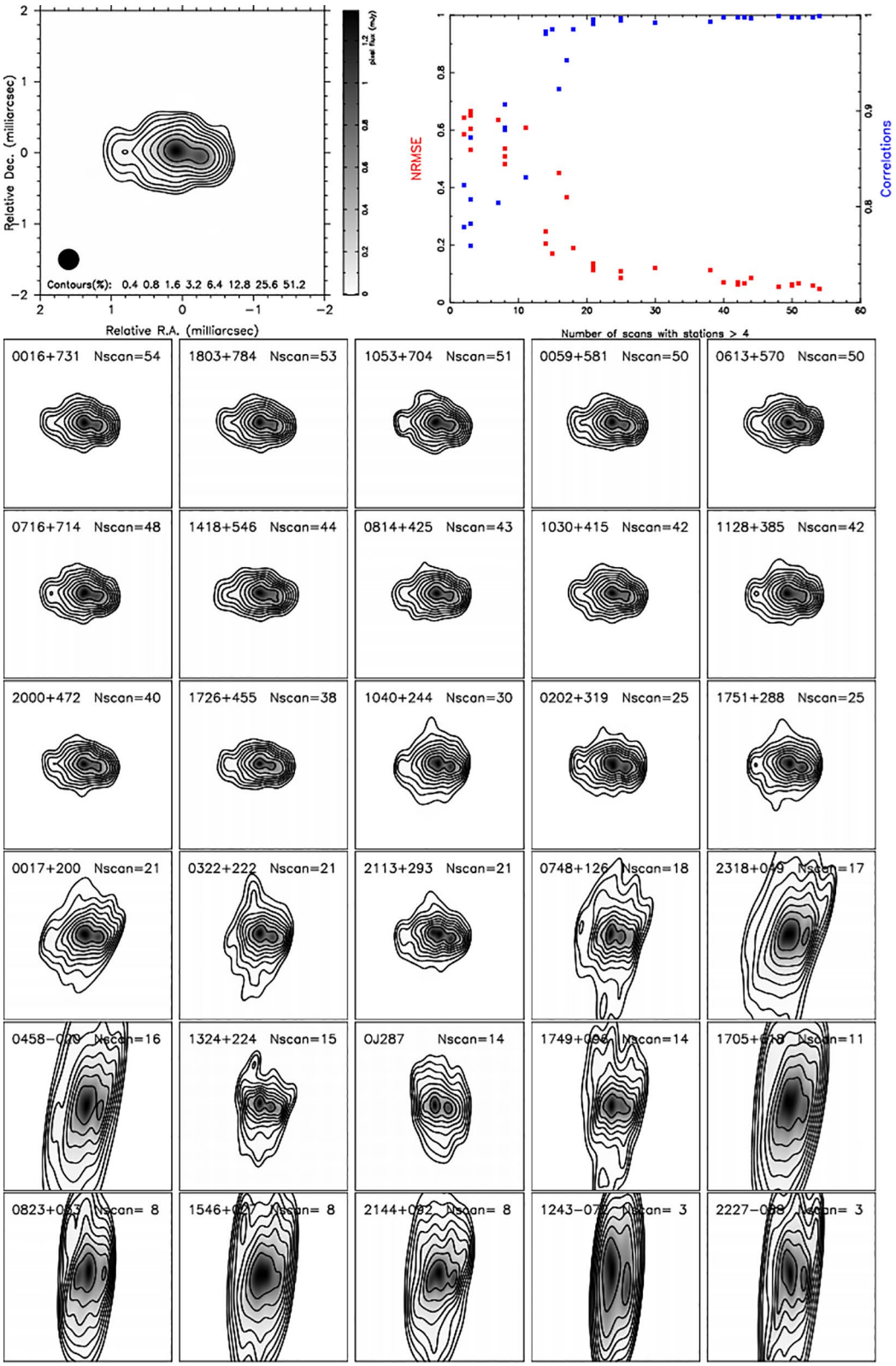
Relative Dec. (milliarcsec)
Relative R.A. (milliarcsec)
Contours(%): 0.4 0.8 1.6 3.2 6.4 12.8 25.6 51.2
NRMSE
Correlations
Number of scans with stations > 4
0016+731 Nscan=54
1803+784 Nscan=53
1053+704 Nscan=51
0059+581 Nscan=50
0613+570 Nscan=50
0716+714 Nscan=48
1418+546 Nscan=44
0814+425 Nscan=43
1030+415 Nscan=42
1128+385 Nscan=42
2000+472 Nscan=40
1726+455 Nscan=38
1040+244 Nscan=30
0202+319 Nscan=25
1751+288 Nscan=25
0017+200 Nscan=21
0322+222 Nscan=21
2113+293 Nscan=21
0748+126 Nscan=18
2318+049 Nscan=17
1324+224 Nscan=15
OJ287 Nscan=14
1705+018 Nscan=11

data sets with more than 10 scans: their NRMSE values change less than 5%, indicating that the imaging process is robust.

2.4. Determining Structure Effects in Broadband Observations

With the derived images at the four bands from VGOS observations, the structure effects in broadband observations can be determined through two steps: (1) calculating the structure phases of the 32 frequency channels deployed in VGOS observations (see Equation A1 in Appendix A1); and (2) performing least square fitting of the structure phases to derive the structure-induced delay, phase at the reference frequency and δTEC, equivalent to the process of producing broadband delays in VGOS (Cappallo, 2014, 2016). We call the second step model fitting. The structure phase at the ith frequency channel, ϕ^{str}_{i}, can be modeled as a function of frequency ν_i as follows:

$$\phi^{str}_{i} = \tau^{str}(\nu_i - \nu_0) + \phi^{str}_{\nu_0} - \frac{\mathbf{k}\,\delta\mathrm{TEC}^{str}}{\nu_i}, \tag{8}$$

where τ^{str}, $\phi^{str}_{\nu_0}$, and $\delta\mathrm{TEC}^{str}$ are the structure effects in broadband delay, phase at $\nu_0 = 6.0$ GHz, and δTEC observables, respectively, and are the three parameters in model fitting. Note that the structure-induced phase at the reference frequency of 6.0 GHz, $\phi^{str}_{\nu_0}$, is determined from least square fitting while the structure phases at the 32 channels in the left-hand side are calculated from images.

Figure 3 shows results of the model fitting process for the second and 44th scans of source 0016 + 731 on baseline GGAO12M-ISHIOKA in session VO0034. The flux-weighted mean positions, which are called mean positions hereafter and are the origins of the images in Figure 5, were used as the reference points to calculate the structure phases of the 32 channels. The uncertainties of the three parameters in Equation 8 were obtained together from least square fitting. Large uncertainties, which indicate a poor fit to the structure phases, can result from large across-band variations in structural phases due to significantly different structure among the four bands or to the misalignment of the images. For the case of source 0016 + 731, the residuals were at the level of a few degrees or even smaller by using the mean positions as the references.

2.5. Selecting Reference Points in the Images at the Four Bands

The reference point in an image is critical in modeling source structure effects because it will immediately affect the derived source position from geodetic VLBI analysis in which the structure models are introduced. In VGOS observations, the reference point requires not only a stable point in the source structure over time but also accurate alignment of the images across the four bands to the actual radio emission of the source. In addition to the mean position previously used, the position of the grid with the peak flux is another reference that is also easily accessible in an image; we call it the peak-flux position. The impact of the alignment can be demonstrated by applying these two types of reference points to derive structure effects and comparing. Figure 4 shows two plots equivalent to those in Figure 3 but using the peak-flux positions for the image alignment.

As we can see from Figures 3 and 4, the modeled structure effects in VGOS group delays, δTEC, and phase offsets at the reference frequency are highly dependent on the reference point used. The residuals of least square fitting for these two cases are also different, which leads to different uncertainties of the three parameters. For source 0016 + 731 the fitting is better, in the sense of smaller residuals, when the mean positions are used as the references. This is the case for many of the sources.

Figure 2. Reconstructed images from the 30 simulated data sets with exactly the same observing schedules as the 30 radio sources in session VO0034, based on the model input image shown for 0642 + 449 in the top-left corner. The 30 images are shown with the same limits of the X/Y axis as the model image. The source names are presented on the top of the 30 images together with the numbers of scans. The images from the simulated data with more than 20 scans of >4 stations have NRMSE of about 0.1 and are consistent with the model. With more than 10 such scans, it is still possible to derive a reasonably good image. NRMSE, normalized root-mean-square error.

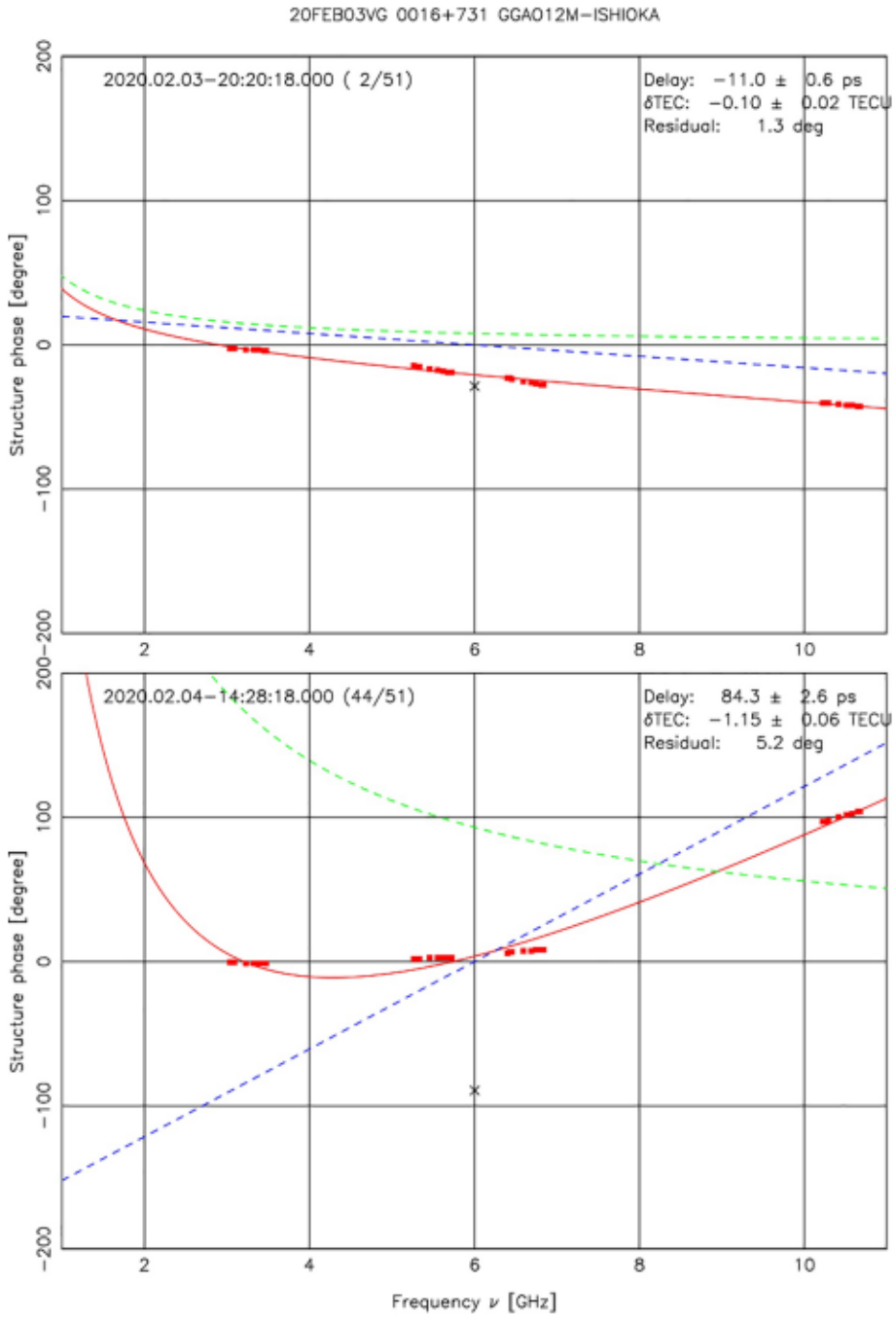

Figure 3. The structure effects on VGOS observables derived through model fitting of the structure phases calculated by using the closure-based images and referring to the mean positions in the images at the four bands. The upper plot is for the second scan of source 0016 + 731 on baseline GGAO12M-ISHIOKA in session VO0034, and the bottom plot for the 44th scan. Structure phases at the 32 channels in red dots are calculated from the images shown in Figure 5. Dashed blue line and dashed green line are the best fit group delay and δTEC model from least square fitting, respectively; black cross on the vertical line of 6.0 GHz is the best fit phase offset. The combined model from these three parameters is shown as the full red line. The estimated values of the structure-induced delays and δTEC are presented in the upper-right corner of each plot together with their uncertainties. The RMS of the postfit residuals are also shown in that corner. VGOS, VLBI Global Observing System; δTEC, total electron content.

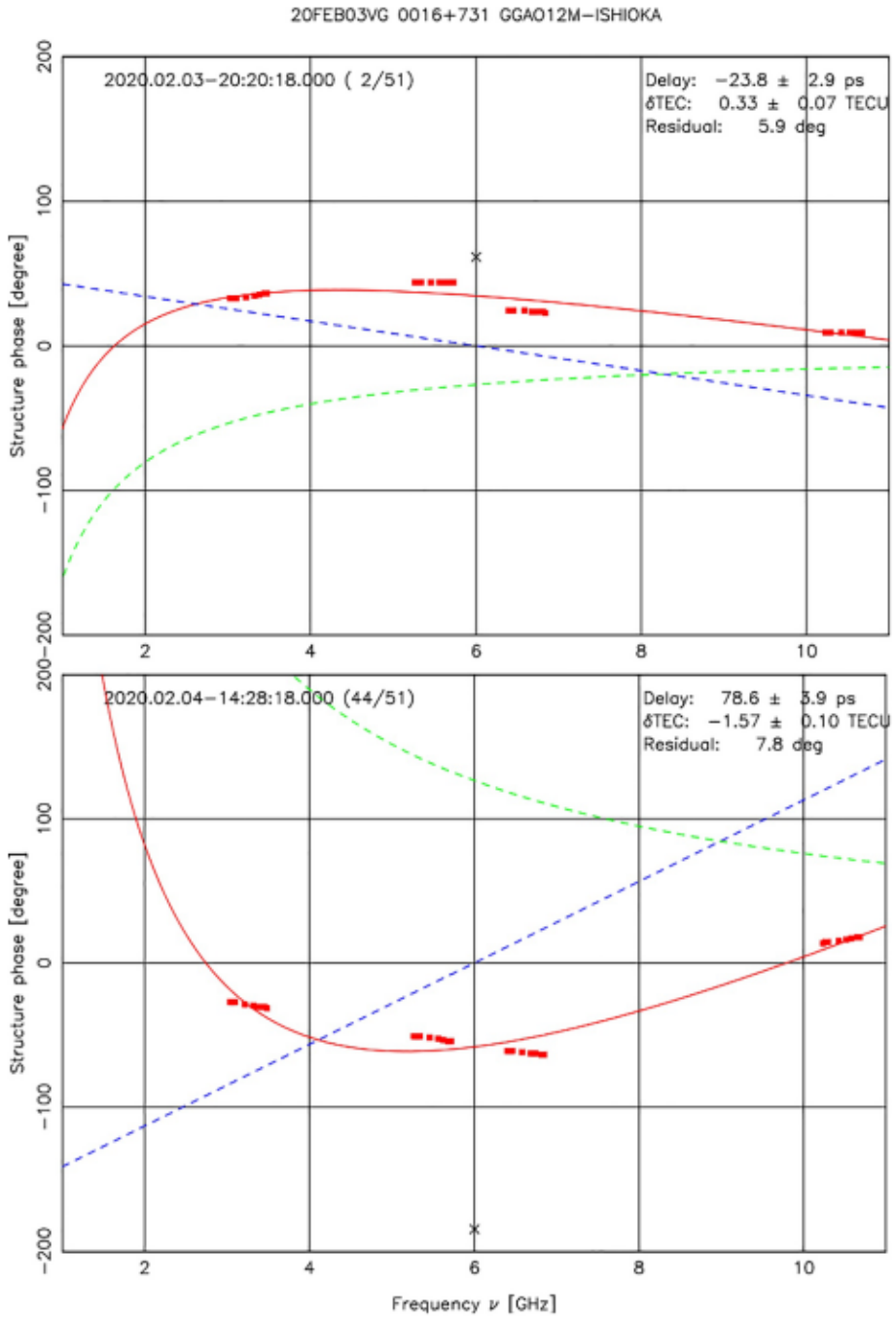

Figure 4. Equivalent plots to Figure 3 but referring to the peak-flux positions in the images to calculate the structure phases at the 32 channels. The coordinates of these reference points are presented in Figure 5. See Figure 3 for a description of the plot.

We note that there is no guarantee that either of these two reference points can align the images at the four bands or be a stable point on the sky over time. The mean positions can change significantly over time and/or from band to band when the structure evolves with time and/or frequency. The peak-flux position can exchange between the jet and the core at different bands and/or times. Meanwhile, due to core shift, which will be discussed in Section 4.2, it is unlikely that the peak-flux position can be used to align the images accurately. However, our study suggests that even though the misalignment of the images at the four bands significantly influences the model fitting, as shown in the previous section, it does not affect the sum of

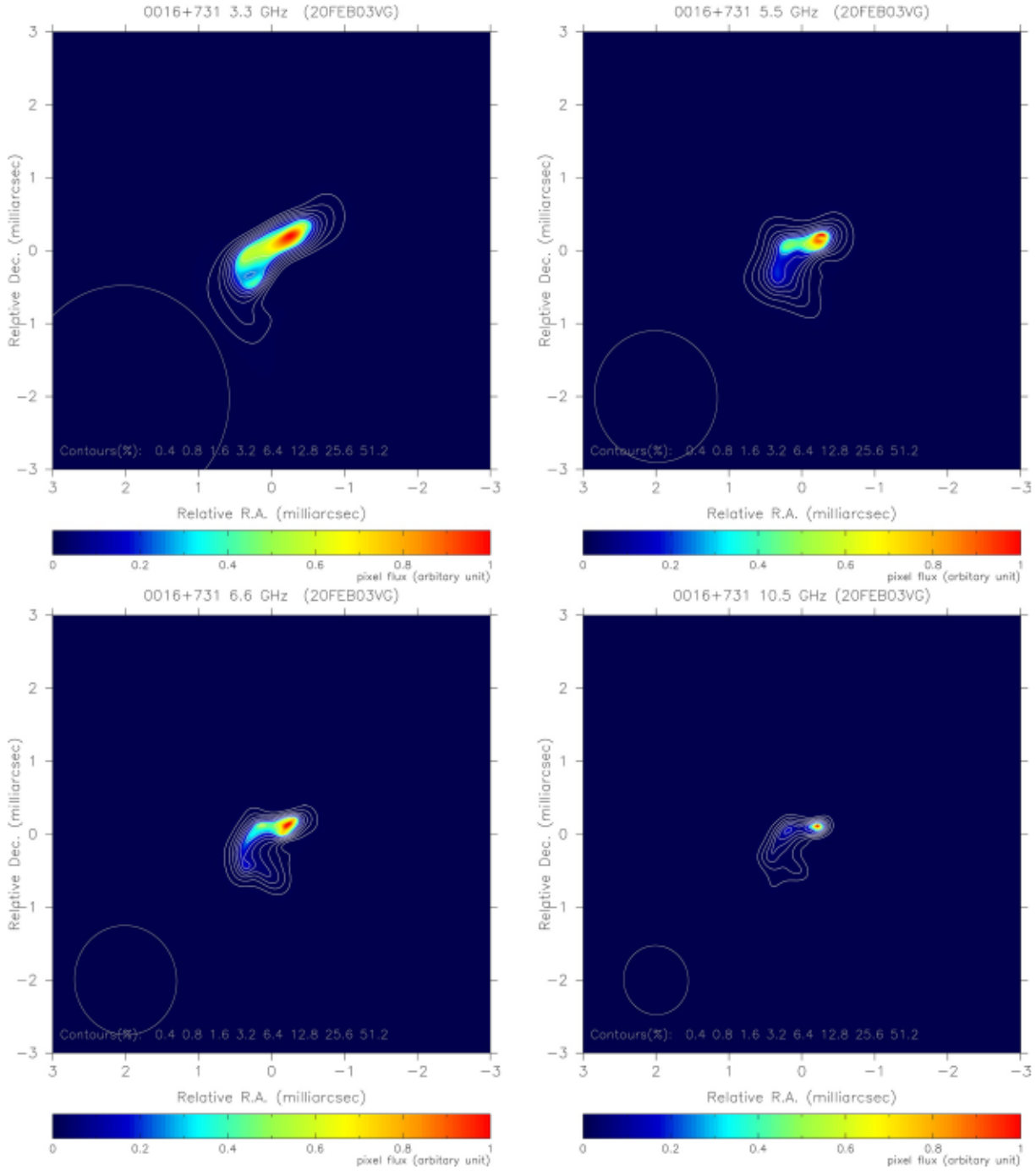

Figure 5. Closure-based images of source 0016 + 731 at the frequencies of 3.3, 5.5, 6.6, and 10.5 GHz from VGOS observations VO0034. Overlay contours are shown at eight levels of peak percentage (specified in the bottom of plots) in white. They were derived based on closure phases and closure amplitudes only, therefore, information of the absolute source positions and the total flux densities was missing. The mean positions were chosen as the centers for the plots and the pixel fluxes are in arbitrary units. The coordinates of the peak are (−0.255, 0.205), (−0.274, 0.206), (−0.224, 0.131), and (−0.208, 0.112) mas in the images at the four bands, respectively. The nominal beam is displayed as a gray ellipse in the bottom-left corner of each plot. VGOS, VLBI Global Observing System.

those model values over a triangle, named modeled closures. Two exceptions to this are that either (or both) of the uncertainties of the modeled closures or the jumps in the modeled closures may change—these will be demonstrated and discussed later. Therefore, we can make use of these two accessible reference points for our analysis here. Please note that for the analysis in the next section, the mean positions were used as the references in the images.

3. Results

3.1. Imaging Results

As an example of moderate structure, the images of source 0016 + 731 obtained from the VGOS session VO0034 are shown in Figure 5. The images show its extended structure at the four bands along the position angle of ~110°. Since VGOS observations at the four frequencies are made simultaneously, their array configuration is the same and therefore the angular scales probed decrease linearly with the increasing frequency. The angular scales of the core decrease when the frequencies go higher; however, the entire structure (the core and the extended jet) has similar extent at the four bands. The structure effects in broadband group delay observables of this source were predominantly due to its structure at higher frequencies; the closure quantities at higher-frequency bands are significantly larger than that at the lowest band as shown in Figures 6 and A1.

These four images were constructed from 645 independent closure phases and 801 independent closure amplitudes at each of the four bands. The reduced χ^2 of the closure phases after removal of the model values is 0.79, 1.12, 1.02, and 1.10 for the four bands, respectively; that of the log closure amplitudes is 1.04, 0.59, 0.86, and 0.89. They are approximately unity suggesting that the fitting was performed well and the uncertainties of the amplitudes and phases were reasonably determined. As a measure of the improvement provided by the imaging results, the root-mean-square (RMS) of the 6,181 (nonindependent) log closure amplitudes at each of the four bands is 0.43 at 3.3 GHz, 0.65 at 5.5 GHz, 0.80 at 6.6 GHz, and 0.87 at 10.5 GHz; after subtracting the modeled log closure amplitudes, the RMS values of the residuals are 0.11, 0.07, 0.08, and 0.12, respectively. Figure 6 shows the observed log closure amplitudes in blue dots and the modeled log closure amplitudes in green open circles for the quadrangle GGAO12M-ISHIOKA-MACGO12M-ONSA13SW. The error bars of observed log closure amplitudes were calculated from the derived uncertainties of amplitude observables on the four baselines of each individual closure as defined by Equation 6. The comparison of closure phases is shown in Appendix A2. Images for seven representative sources are shown in Appendix A3.

Direct comparisons of the VGOS images at the four bands with the corresponding MOJAVE image, shown in Appendix A4, were made for six sources. These MOJAVE images were obtained by astronomical arrays that have a good calibration and good (u, v) coverage. For the comparison, the VGOS images were constrained to have the same total flux densities as the corresponding MOJAVE images.

Since images with different resolutions contain structure at different angular scales, we used the Gaussian beams of two different sizes to convolve both the VGOS images and MOJAVE images before the image comparison: the full-beam size of the VGOS image under investigation and one fifth of that beam size. The full-beam resolution allows us to compare large-scale structure whereas the over-resolved approach can tell the difference in fine-scale structure. The cross correlation and NRMSE values of the comparison for the full-beam size convolved images are shown in Table 1. In this case, the correlation is often very high, larger than 0.95, and around half of the VGOS images have NRMSE values of 0.2 or smaller. It suggests that at large scales the VGOS images are consistent with the MOJAVE images. In general, the NRMSE values for VGOS images at higher frequencies are significantly larger than that for the ones at lower frequencies, probably mainly due to the finer angular resolutions at the higher frequencies. Table 2 shows the results of comparing the images convolved with the smaller beam sizes. In this case, all the NRMSE values are significantly larger than 0.2, which says that they have quite different structure at fine scales. If we take source 1030 + 415 as an example, the MOJAVE image shows only a dominant core, while the VGOS images at the two higher-frequency bands clearly reveal it has a strong jet away from the core by an angular distance of approximately the beam size; we will discuss in the next subsection further the strong structure effects caused by its structure within the beam size.

The VGOS images were consistent with the MOJAVE images when convolved with the full-beam sizes, but were significantly different when convolved with much smaller beam sizes. There are two possible reasons: (1) the RML algorithm is better at deriving images with higher resolutions or (2) radio sources have more prominent jet structure at the lower frequency bands, which is always true for synchrotron jets. Therefore, the NRMSE values were much smaller when the large-scale structure was compared, and they considerably increased when the fine-scale structure was evaluated. However, by comparing the structure phases

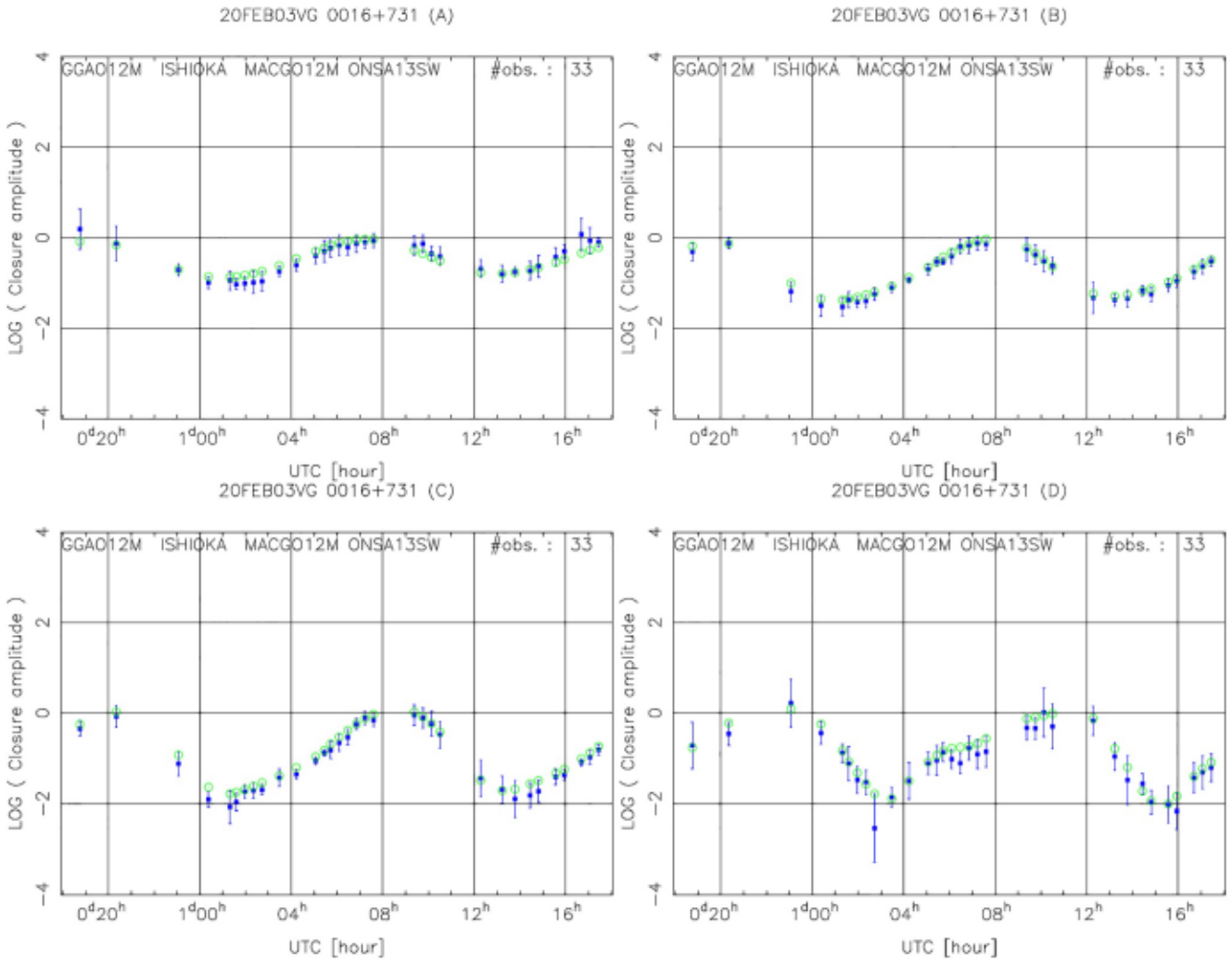

Figure 6. Observed log closure amplitudes (blue dots) and modeled log closure amplitudes (green open circles) of quadrangle GGAO12M-ISHIOKA-MACGO12M-ONSA13SW for source 0016 + 731 at the frequencies 3.3 GHz (upper-left), 5.5 GHz (upper-right), 6.6 GHz (bottom-left), and 10.5 GHz (bottom-right) in session VO0034. The RMS values of the log closure amplitudes of this quadrangle are 0.58, 0.94, 1.24, and 1.18 at the four bands, respectively; after subtracting the modeled log closure amplitudes, the corresponding RMS values of the residuals are 0.15, 0.08, 0.15, and 0.16. RMS, root-mean-square.

calculated based on the images convolved with these two different beam sizes, it is found that the fine-scale structure is important for VGOS observations to model source structure effects, as already discussed by Porcas (2010).

3.2. Closure Delays

Using the constructed images at the four bands and model fitting, structure-induced delays, δTEC, and phase offsets at 6.0 GHz were determined together with their uncertainties. They were used to calculate modeled closures, which were compared with the observed closures. The comparisons of closures temporarily avoid the difficulty of properly aligning the images.

3.2.1. Source 0016 + 731

For the 1,883 closure delays of source 0016 + 731 in session VO0034, the RMS is 24.9 ps; after subtracting the modeled closure delays, it reduces to only 5.5 ps. A magnitude of 24.3 ps in the variation of the observed closure delays for this source is explained by its structure effects. Figure 7 shows its observed and modeled

Table 1
Statistics of the Comparison Between Our Results and MOJAVE Images When Both are Convolved With the Corresponding Beam Sizes of VGOS Images

	3.3 GHz		5.5 GHz		6.6 GHz		10.5 GHz	
Source	Corr.	NRMSE	Corr.	NRMSE	Corr.	NRMSE	Corr.	NRMSE
0016 + 731	0.998	0.09	0.990	0.17	0.984	0.20	0.958	0.31
0642 + 449	0.995	0.13	0.975	0.25	0.960	0.31	0.910	0.43
1030 + 415	0.999	0.07	0.997	0.13	0.995	0.16	0.986	0.24
1418 + 546	0.970	0.28	0.968	0.29	0.964	0.31	0.946	0.37
1803 + 784	0.994	0.13	0.983	0.21	0.979	0.23	0.971	0.27
3C418	0.985	0.24	0.950	0.40	0.916	0.47	0.812	0.63

closure delays for two triangles GGAO12M-ISHIOKA-ONSA13SW and ISHIOKA-MACGO12M-ONSA13SW as examples to demonstrate this.

Similar to the closures from the traditional S/X VLBI observations, the closures of broadband group delays determined from the process in Section 2.4 have the feature that they are insensitive to the reference points in source structure at any of the four bands. Even though closure delays involve three baselines, which leads to difficulty in interpretation of source structure effects, they are still instructive to understand those effects on each of the three baselines. There are three pairs of positive and negative peaks separated by 12 h in both plots; each of the three pairs of positive and negative peaks correspond to the structure effects on each of the three baselines. The structure effects of source 0016 + 731 cause errors on the baselines in the plots with magnitudes of about 50 ps, which do not include the effects of a possible source position shift due to its structure.

3.2.2. Source 1030 + 415

The images of source 1030 + 415 are shown in Figure A8. At the three higher frequencies, two components separated by ∼1 mas are visible. The relative flux ratio of the two components gets stronger when the frequency increases, which leads to much larger structure effects at higher-frequency bands. For its 813 closure delays in the session VO0034, the RMS is 50.2 ps, and the RMS residual is 10.1 ps after correction based on the images. Significant amount of systematic errors due to structure effects is removed by using the images. Figure 8 shows the structure effects on triangle KOKEE12M-ONSA13SW-WESTFORD. The model curve predicts well the observed closure delays. It has larger and more complicated structure effects compared to source 0016 + 731.

There are two jumps in closure delays at about 09:00 and 13:00 UTC, as indicated by the continuous model curve. They are caused by shifts of 2π in the structure phases at 10.5 GHz before those two epochs, which can be demonstrated by the structure phases from the images. The jumps will be studied further in Section 3.4.

Table 2
Statistics of the Comparison Between Our Results and MOJAVE Images When Both are Convolved With One Fifth of the Corresponding Beam Sizes of VGOS Images

	3.3 GHz		5.5 GHz		6.6 GHz		10.5 GHz	
Source	Corr.	NRMSE	Corr.	NRMSE	Corr.	NRMSE	Corr.	NRMSE
0016 + 731	0.922	0.40	0.890	0.47	0.882	0.48	0.869	0.50
0642 + 449	0.856	0.52	0.800	0.60	0.793	0.61	0.785	0.62
1030 + 415	0.962	0.34	0.918	0.44	0.903	0.48	0.875	0.52
1418 + 546	0.928	0.41	0.913	0.45	0.910	0.46	0.903	0.47
1803 + 784	0.959	0.30	0.939	0.35	0.932	0.37	0.914	0.41
3C418	0.757	0.70	0.711	0.74	0.697	0.75	0.670	0.77

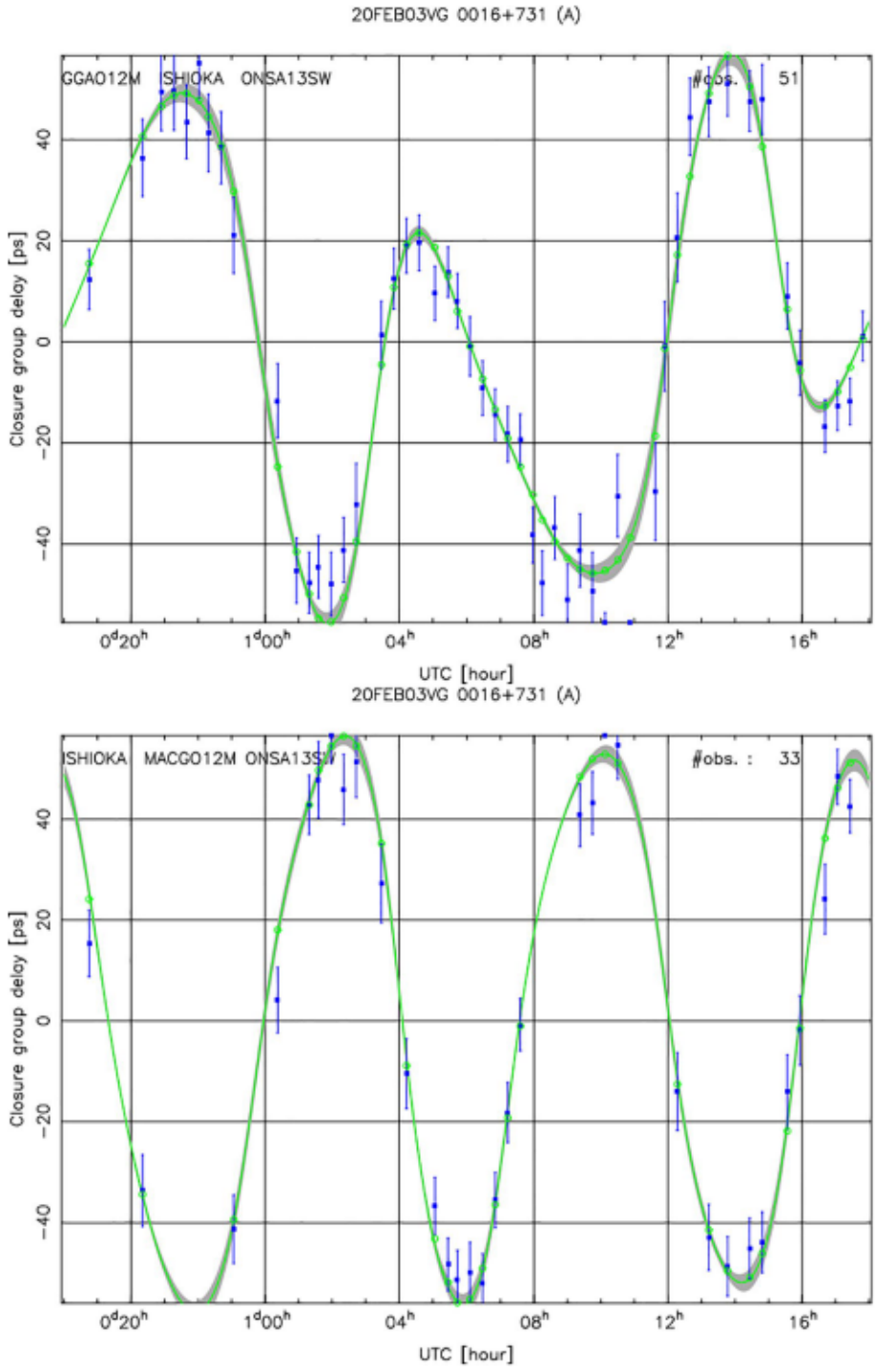

Figure 7. Observed closure delays (blue dots) and modeled closure delays (green open circles) of two triangles GGAO12M-ISHIOKA-ONSA13SW (upper) and ISHIOKA-MACGO12M-ONSA13SW (bottom) for source 0016 + 731 in session VO0034. The continuous model curve is shown as the green line and the 1-σ errors are in gray. The RMS closure delays of these two triangles are 34.2 ps (upper) and 40.5 ps (bottom), and the RMS of the residuals for both is 6.5 ps. RMS, root-mean-square.

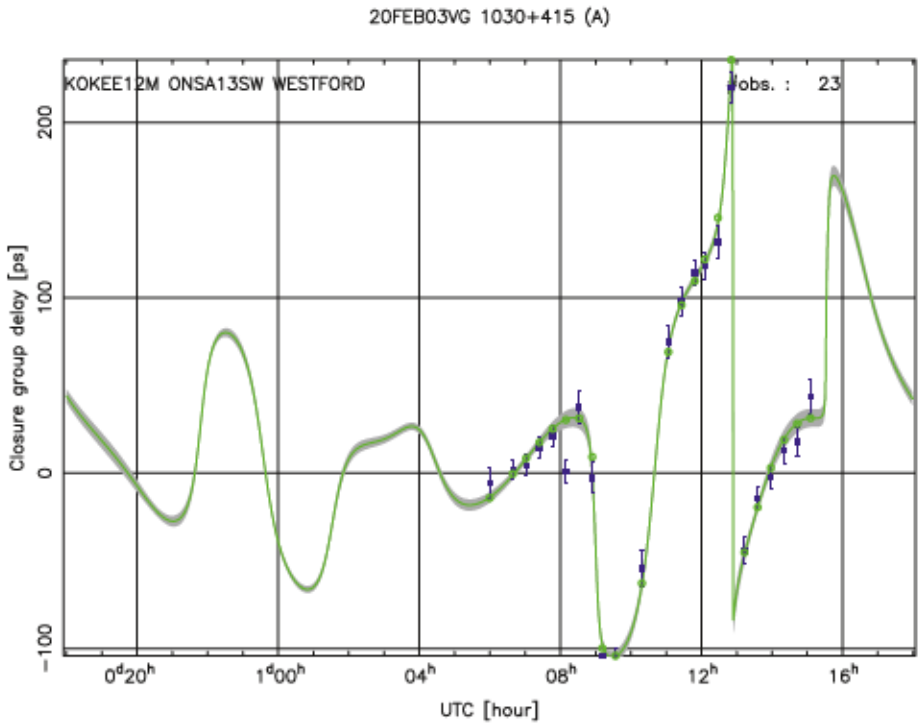

Figure 8. Observed closure delays (blue dots) and modeled closure delays (green open circles) of triangle KOKEE12M-ONSA13SW-WESTFORD for source 1030 + 415 in session VO0034. The continuous model curve is shown as the green line and the 1-σ errors are in gray. The RMS closure delay of this triangle is 78.7 ps, and the RMS residual is 10.1 ps after subtracting the modeled closure delays. There are two jumps in closure delays with magnitudes of more than 100 ps at about 09:00 and 13:00 UTC. RMS, root-mean-square.

3.3. Closure δTEC

The sum of δTEC estimates over a loop of three stations, called closure δTEC, uncovers systematic errors in δTEC estimates. The ionospheric effects are station-based, and thus are closed along the loop of a triangle. Since the effects of source structure are frequency-dependent and so far are not corrected in channel visibility phases, the actual δTEC observables are affected by these effects, causing nonzero closure δTEC values. Using our imaging results, source structure effects on δTEC can also be studied and quantified by forming modeled closure δTEC. Figure 9 shows the observed closure δTEC and modeled closure δTEC on the triangle ISHIOKA-WESTFORD-WETTZ13S for source 1418 + 546 and on the triangle ISHIOKA-KOKEE12M-WETTZ13S for source 1803 + 784. Note that modeled closure δTEC is the negative of the sum of structure-induced δTEC on three baselines based on Equation 8 in order to follow the sign of the observed closure δTEC. The images of these two sources are shown in Figures A9 and A2, respectively. The systematic errors in δTEC observables from VGOS observations can be significantly reduced by correcting for source structure effects. As we have seen, it is common that structure effects cause systematic errors at the level of one TECU on VGOS δTEC observables. Attention must be paid to use of these δTEC observables.

3.4. Delay/δTEC Jumps

Jumps in the delay and δTEC observables were reported by Xu et al. (2020). These jumps are confirmed to be caused by source structure effects in this study by comparing observed closures to modeled closures. Taking as an example, Figure 10 shows observed and modeled closure delays of triangle GGAO12M-ONSA13SW-RAEGYEB for source 3C418 in session VT9217, the images of which are shown in Figure A6. When uncertainties of the modeled closure delays are smaller than about 10 ps, the modeled closure delays agree with the observed ones very well. However, when uncertainties of the modeled

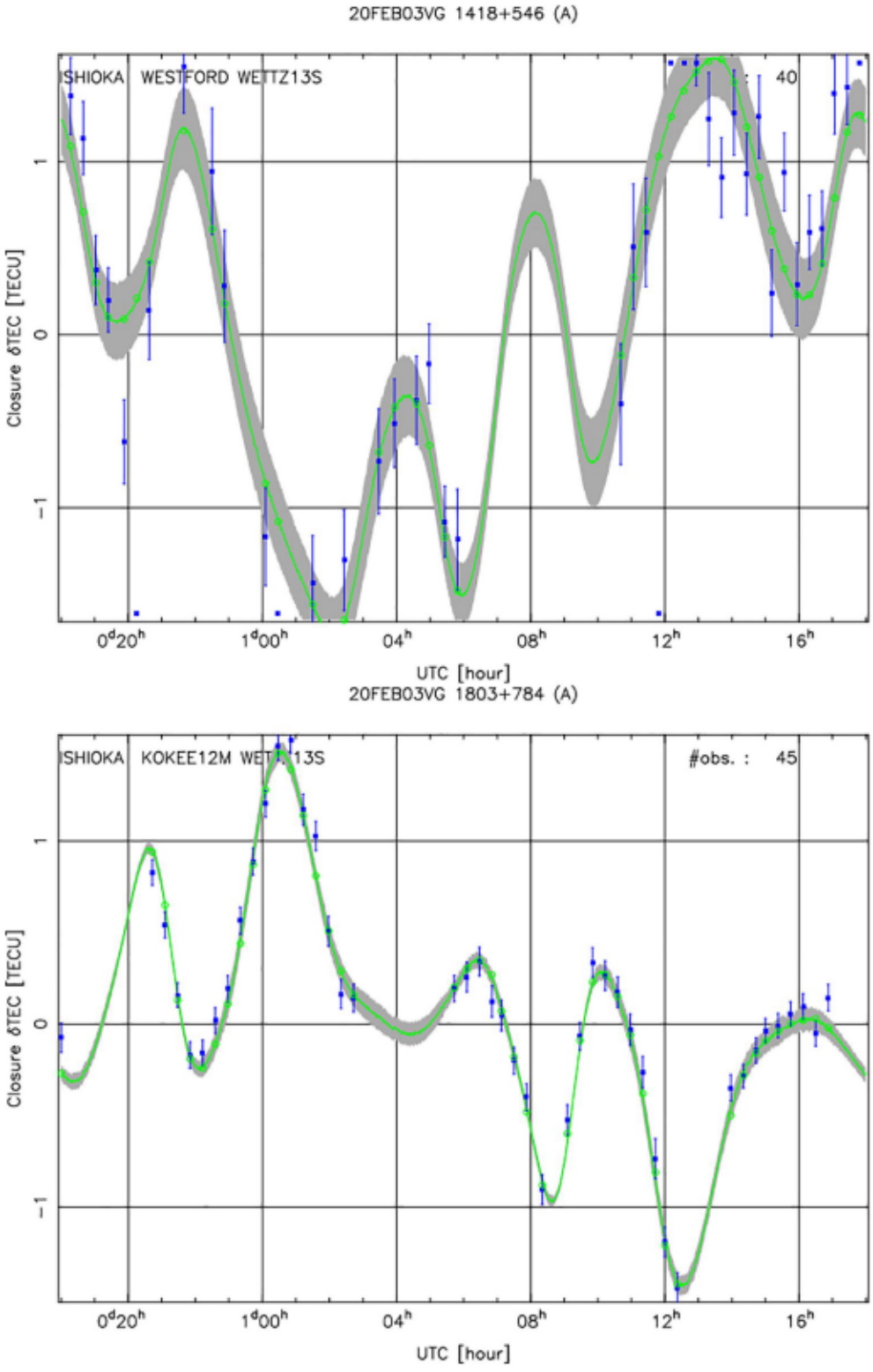

Figure 9. Observed closure δTEC (blue dots) and modeled closure δTEC (green open circles) of triangle ISHIOKA-WESTFORD-WETTZ13S for source 1418 + 546 (upper) and of triangle ISHIOKA-KOKEE12M-WETTZ13S for source 1803 + 784 (bottom) in session VO0034. The continuous model curve is shown as the green line and the 1-σ errors are in gray. The RMS values of closure δTEC are 1.10 TECU (upper) and 0.62 TECU (bottom), and the RMS residuals are 0.39 TECU (upper) and 0.09 TECU (bottom). δTEC, total electron content.

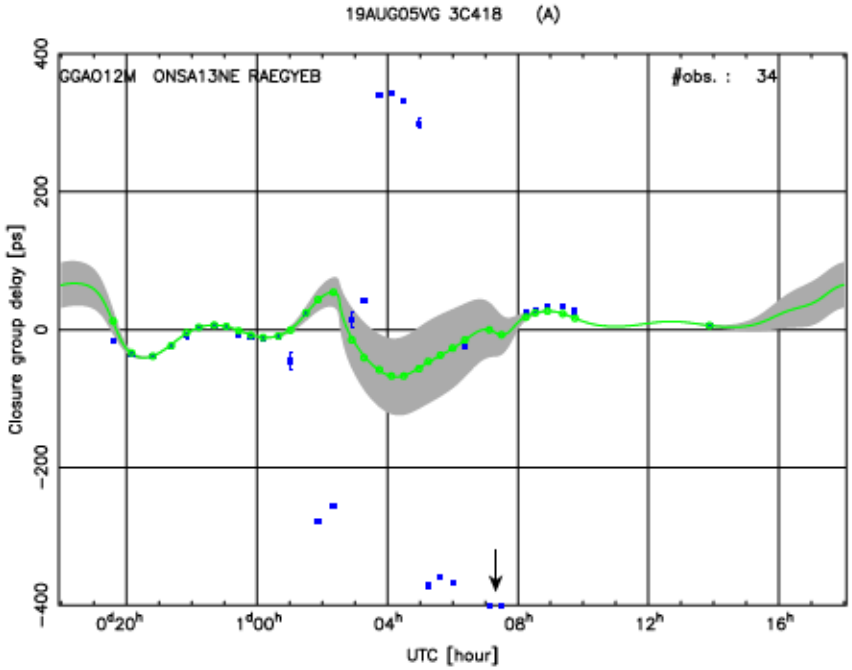

Figure 10. Observed closure delays (blue dots) and modeled closure delays (green open circles) of triangle GGAO12M-ONSA13SW-RAEGYEB for source 3C418 in session VT9217. The continuous model curve is shown as the green line and the 1-σ errors are in gray. Two observed closure delays of about −720 ps, pointed by the arrow, are shown on the bottom axis.

values are large, the observed closure delays deviate from the modeled ones by several hundreds of picoseconds.

These jumps are found to be caused by large variations in phases among the four bands due to source structure effects. In the cases of extended sources, the frequency separations between the four bands are large enough for their structure effects to produce phase differences larger than 2π between various bands. Without correcting structure phases in the process of producing VGOS broadband delay and δTEC, such phase ambiguities among the four bands may not be successfully resolved. Model fitting to the structure phases on baseline GGAO12M-ONSA13NE for one of the scans with delay jumps shown in Figure 10 is demonstrated in Figure 11. There are three possibilities to do model fitting for this scan: (1) wrapping all the phases to the range −180° to 180° (the upper plot); (2) shifting the phases at the second band by −360° (the middle one); and (3) shifting the phases at the third band by 360° (the bottom one). The difference in delay estimates between the first and second scenarios is about −355 ps and that between the first and third scenarios is about 327 ps. Since the triangle GGAO12M-ONSA13SW-RAEGYEB involves another long baseline, GGAO12M-RAEGYEB, the jumps in its closure delays can have spacing with various combinations of those two values or two times one of them. More complicated jumps are found in closure delays for larger triangles. Delay jumps in the observations of other sources like 0642 + 449, 1030 + 415, 1418 + 546, and 2000 + 472 are explained by their structure effects as well. Their images are shown in Figures A7–A10, respectively. The jumps in δTEC observables are caused by the same reason. It is likely that those observations with large jumps could be recovered for use in geodetic solutions if structure phases were taken into account in the VGOS data processing.

4. Discussion

4.1. Impact of the Reference Points in Source Structure

By referring to a different point in the image for each of the four bands, the model fitting gives completely different model values; however, the closure values remain unchanged except when the jumps in the mod-

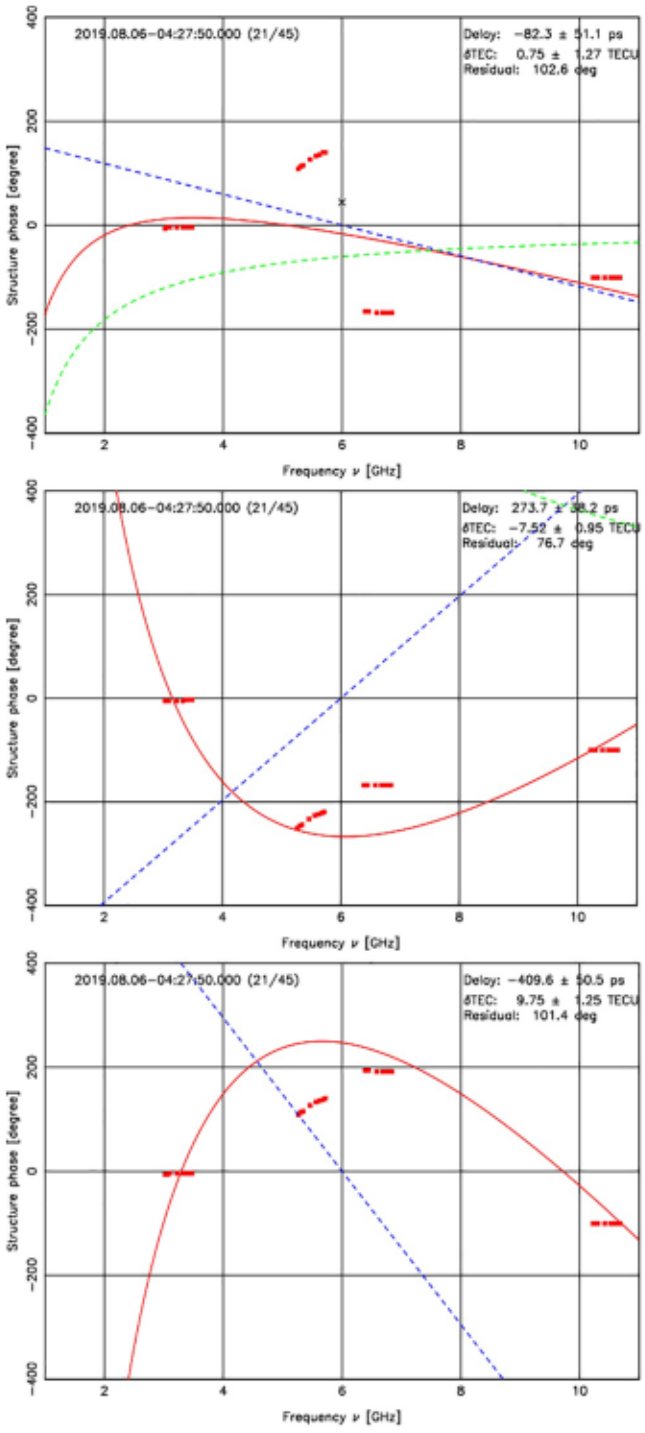

Figure 11. Three possible scenarios of model fitting to the structure phases at the 32 channels on baseline GGAO12M-ONSA13NE for the 21 scan of the source 3C418 in session VT9217. The case of wrapping the structure phases to the range −180° to 180° is shown in the upper plot. The middle plot is the case of shifting the structure phases change at of the eight channels around 5.5 GHz by −360°, and the bottom one shifting the structure phases of the eight channels around 6.6 GHz by 360°. This large variation in structure phases leads to unpredictable jumps in delay and δTEC observables. See Figure 3 for the plot design.

eled delay/δTEC values occur. The reason is that the differences between the model values of structure-induced delays when using different reference points form sinusoidal waves, which can be modeled by a common source position offset for all the baselines and thus be canceled out exactly in closures. This is shown in Figure 12 for the images of sources 0016 + 731 and 1030 + 415. The differences between the model values for the observations of source 0016 + 731 on the 27 baselines in session VO0034 can be modeled perfectly by a position offset of (−0.393, −0.005) mas and those of source 1030 + 415 by a position offset of (2.658, −0.784) mas. Neither of these two cases can be easily inferred from the position offsets between the two types of reference points used. The misalignment between the images at the four bands would cause variations in derived source positions from geodetic VLBI solutions. The dependence of the source position determined by broadband group delays on the reference points of the images at the four bands requires further investigations (Xu et al., in preparation). Due to the strong correlation between broadband delays and δTEC (Cappallo, 2015; Xu et al., 2020), systematic differences with the same pattern as the differences in modeled broadband delays will happen to modeled δTEC values; thus, external information on δTEC with an accuracy better than 0.5 TECU may help in aligning the images (Xu et al., in preparation).

For sources with moderate structure, if the jet position angles at various bands are along the same direction, which is validated for most of radio sources (see http://www.physics.purdue.edu/astro/MOJAVE/ for the MOJAVE images), the structure phases at the 32 channels are always in phase by referring to the mean positions—zero structure phases at the four bands tend to happen at the same epochs as well as the maximum and minimum phases. This in-phase feature leads to a good model fitting and thus small uncertainties of the parameters as shown in Figure 3. But the choices of other reference points result in additional phase offsets between the four bands, leading to structure phases at the 32 channels that are out of phase and thus to larger uncertainties of the parameters. For sources with complicated structure, the structure phases at the 32 channels in the four bands are generally not consistent with a delay/phase offset/δTEC model even when referring to the mean positions, as we can see in Figures 10 and 11. The large variations in structure phases at different bands, which cause the jumps, may happen at different periods of time if referring to different reference points. However, apart from the jumps, the modeled closures of the extended sources do not change with the different reference points used.

4.2. Core Shift

What we call the "core" in the VLBI images of active galactic nuclei jets at centimeter wavelengths is in fact the synchrotron photosphere, that is, the point at which the jet becomes optically thin at the given frequency. As predicted by Blandford and Königl (1979) the position of the core along the jet is frequency-dependent with the core moving upstream with increasing frequency. The effect has been measured by using quasi-simultaneous multifrequency VLBI observations (e.g., Kovalev et al., 2008; Plavin et al., 2019; Pushkarev et al., 2012; Sokolovsky et al., 2011). The frequency-dependency of the core position can be parameterized by $k\nu^{-\beta}$, where k is a source-dependent core shift parameter,

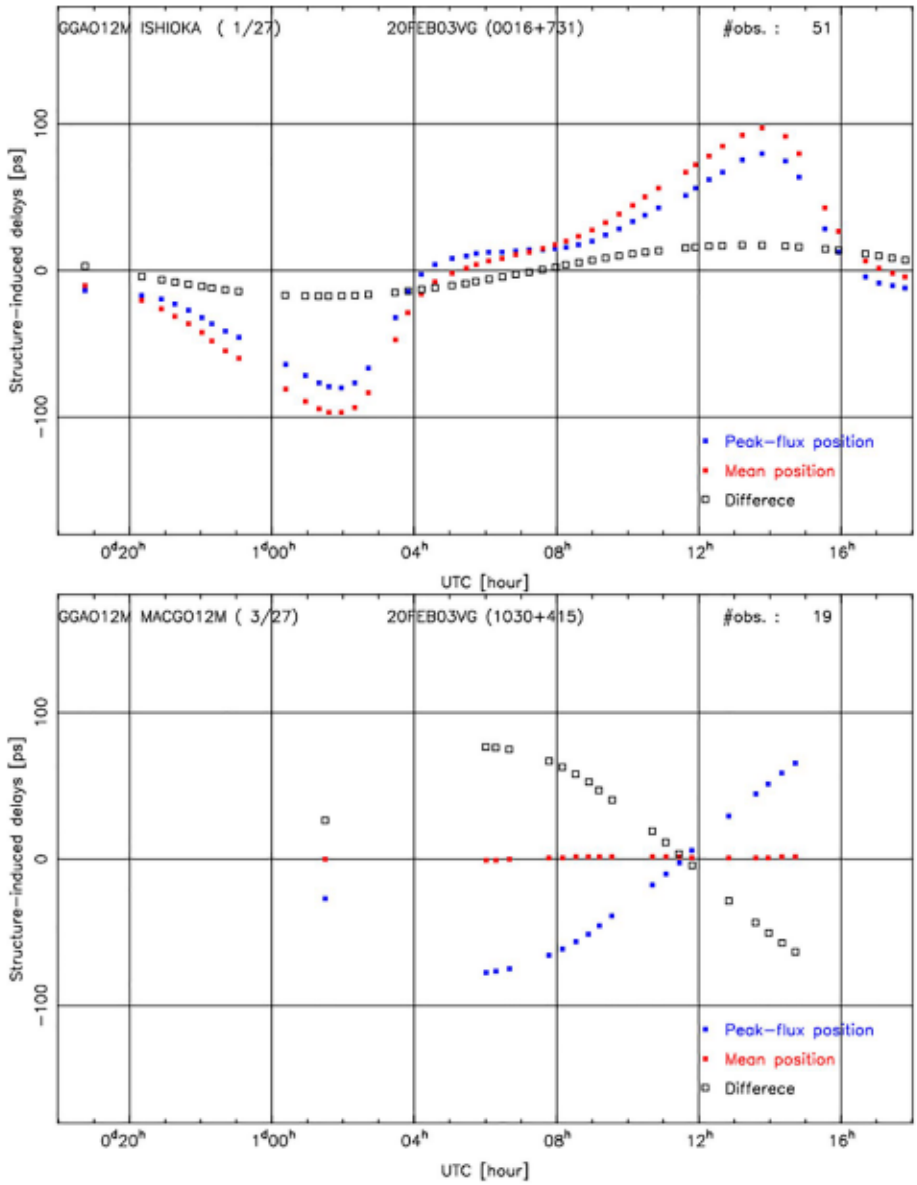

Figure 12. Structure-induced delays in VGOS broadband observations of source 0016 + 731 (upper) and of source 1030 + 415 (bottom) based on registering the images at the four bands to the peak-flux positions (blue dots) and to the mean positions (red dots). The differences between them are shown in black rectangles. VGOS, VLBI Global Observing System.

ν is the observing frequency, and β is an astrophysical parameter. So far, β is measured to be close to 1 (Lobanov, 1998; Sokolovsky et al., 2011). Since the core changes its position as a function of the observing frequency due to core shift, it must be taken into account when aligning the images at the four bands; it can be very challenging to determine this effect with a precision of better than 100 μas in the frequency range of VGOS. The effects due to the relative angular structure are determined as shown in the imaging results, and the remaining part of the core shift effect is equivalent to a shift in the absolute source position between the four bands. The latter was discussed in Appendix A.

We performed a series of simulations with different dependency of the core shift on the observing frequency for several sources in this study; the results confirm that if β equals 1, the impact of core shift

is not present in any closure quantities or in the baseline-based group delay or δTEC observables, but does lead to a source position shift when analyzed with baseline-based phase delays. As discussed by Porcas (2009), when β is about one and the source has merely a compact core, group delays measure the source position at the jet base rather than the actual location where the radio signals were emitted and which the phase observables measure. This conclusion is also valid for sources with complex structure when the effects of the relative structure in group delays and phase delays are modeled in advance. Therefore, by using the differences between the broadband group delays and phase delays from VGOS, it is possible to determine the core shift with high accuracy. If β deviates from 1, it will cause variations in baseline-based δTEC observables. In other words, external information about the dispersive effects that has uncertainties comparable to the broadband δTEC observables may allow us to detect the part of core shift deviating from $\beta = 1$, if any. The study of detecting core shift from VGOS observations based on these possibilities is in progress.

From astrophysical observations, the radio core shift was determined for a number of sources by referring to bright compact features in the optically thin, extended jet. This method is named "self-referencing" technique and has been used in a series of studies (e.g., Kovalev et al., 2008; Plavin et al., 2019; Pushkarev et al., 2012; Sokolovsky et al., 2011). Relative astrometrical VLBI, the so-called phase referencing technique, nowadays approaches relative positional accuracies at the level of 10 μas (Reid & Honma, 2014). By using this high precision technique, a handful of radio sources have been observed to measure their core shift (e.g., Dodson et al., 2017; Martí-Vidal et al., 2011; Rioja et al., 2015; Ros et al., 2001). Moreover, it has been shown that by applying a method of multifrequency phase referencing, there is no need to observe any calibrator source and the observing time per source can be significantly reduced (Dodson et al., 2017). Both the self-referencing technique applied to our VGOS images and the phase referencing technique with external VLBI observations should be explored to investigate the core shift of VGOS sources.

5. Conclusions

We have made images of extragalactic radio sources at the frequencies of 3.3, 5.5, 6.6, and 10.5 GHz based only on closure phases and closure amplitudes from VGOS broadband observations. A model fitting process equivalent to that used in producing broadband delay and δTEC observables was applied to derive structure-induced delays and δTEC, which were used to obtain modeled closures. These closures were compared with the observed ones. Structure effects in VGOS observations and the jumps in delays and δTEC observables were investigated in detail. Finally, we discussed the alignment of the images at the four bands.

We tested the fidelity of our image reconstruction method by using simulated data with a known ground truth model and a (u, v) coverage and thermal noise properties identical to the actual VGOS observations. Closure-only imaging was demonstrated to be robust, and it produced consistent images for the sources with observations of more than 12 scans. With about 1,100 scans and 80 sources in one 24-h VGOS session, on average each source can have more than 12 scans. The IVS VGOS Technical Committee (see https://ivscc.gsfc.nasa.gov/about/com/vtc/index.html) is working on reducing the integration time of an observation to 10 s from the 30 s used at present. The number of scans in a session is expected to be more than doubled. These changes are promising for deriving images for a large number of sources from the VGOS observations with a good quality and a long time series in the VGOS era.

The closure-only images from the actual VGOS data predict source structure effects in broadband delays and δTEC very well. For the cases of sources 0016 + 731 and 1030 + 415, the RMS closure delays were 24.9 and 50.2 ps in session VO0034, respectively; after correcting for source structure effects the RMS residuals were reduced to 5.5 and 10.1 ps. It was demonstrated that structure effects in broadband delays were dominated by source structure at higher frequencies, while those at the lowest frequency band were suppressed. The systematic errors in δTEC observables as shown in closure δTEC were also explained by these effects. Our study revealed that the jumps in delay and δTEC observables were caused by 2π phase shifts among the

four bands due to strong source structure effects. They can be resolved when the structure effects are taken into account. A big improvement in geodetic VLBI solution is expected by correcting these effects, and the study on this topic is in progress.

The absolute source position and the total flux density are completely missed in the closure-only images. The main difficulty in correcting source structure effects is to identify the reference points in the images at the four bands in order to maintain stable source positions over time. External δTEC estimates with high accuracy may help to verify the reference points in the images and even determine core shift effects. The technique of self-referencing applied to VGOS images and external VLBI phase referencing measurements may also play an important role in determining these effects.

Based on this study, we argue that it is critical for VGOS observations to take source structure effects into account already in the postcorrelation process and the observation scheduling in order to minimize the random and systematic error contributions from these effects.

Appendix A

A1. Models of Source Structure Effects

Consider that a source has an image at the frequency ν with N components and the flux of the ith component is A_i. In this study, the images have 360,000 components. An arbitrary point in the image, O, is selected as the reference to describe the relative position of the ith component, $\bar{k}_i$. The phase due to structure effect of this source on a baseline with the (u, v) vector of $\bar{b}$ is written as

$$\phi_\nu^{\mathrm{str}} = \tan^{-1}\frac{\sum_{i=1}^{N} A_i \cos(2\pi\nu\bar{k}_i \cdot \bar{b} / c)}{\sum_{i=1}^{N} A_i \sin(2\pi\nu\bar{k}_i \cdot \bar{b} / c)}, \tag{A1}$$

where c is the speed of light.

The delay at a specific frequency ν due to source structure is given by

$$\tau_\nu^{\mathrm{str}} = \frac{\partial\phi_\nu^{\mathrm{str}}}{\partial\nu}. \tag{A2}$$

The observed amplitude, $\mathbf{V}_\nu^{\mathrm{str}}$ is given as follows:

$$V_\nu^{\mathrm{str}} = \sqrt{\left[\sum_{i=1}^{N} A_i \cos(2\pi\nu\bar{k}_i \cdot \bar{b} / c)\right]^2 + \left[\sum_{i=1}^{N} A_i \sin(2\pi\nu\bar{k}_i \cdot \bar{b} / c)\right]^2}. \tag{A3}$$

A2. Closure Phases of Source 0016 + 731

In total, source 0016 + 731 has 1879 closure phases in session VO0034 with RMS values of 4.5° at 3.3 GHz, 9.7° at 5.5 GHz, 17.3° at 6.6 GHz, and 30.4° at 10.5 GHz. After subtracting the modeled closure phases from the observed ones, the RMS values of the residuals are 4.4°, 4.1°, 4.8°, and 6.5° at the four bands, respectively. Figure A1 shows the closure phases of triangle GGAO12M-ISHIOKA-WETTZ13S from actual observations in blue dots and from the derived images in green open circles. The error bars of observed closure phases are calculated from the derived uncertainties of phases on the three baselines of each individual closure.

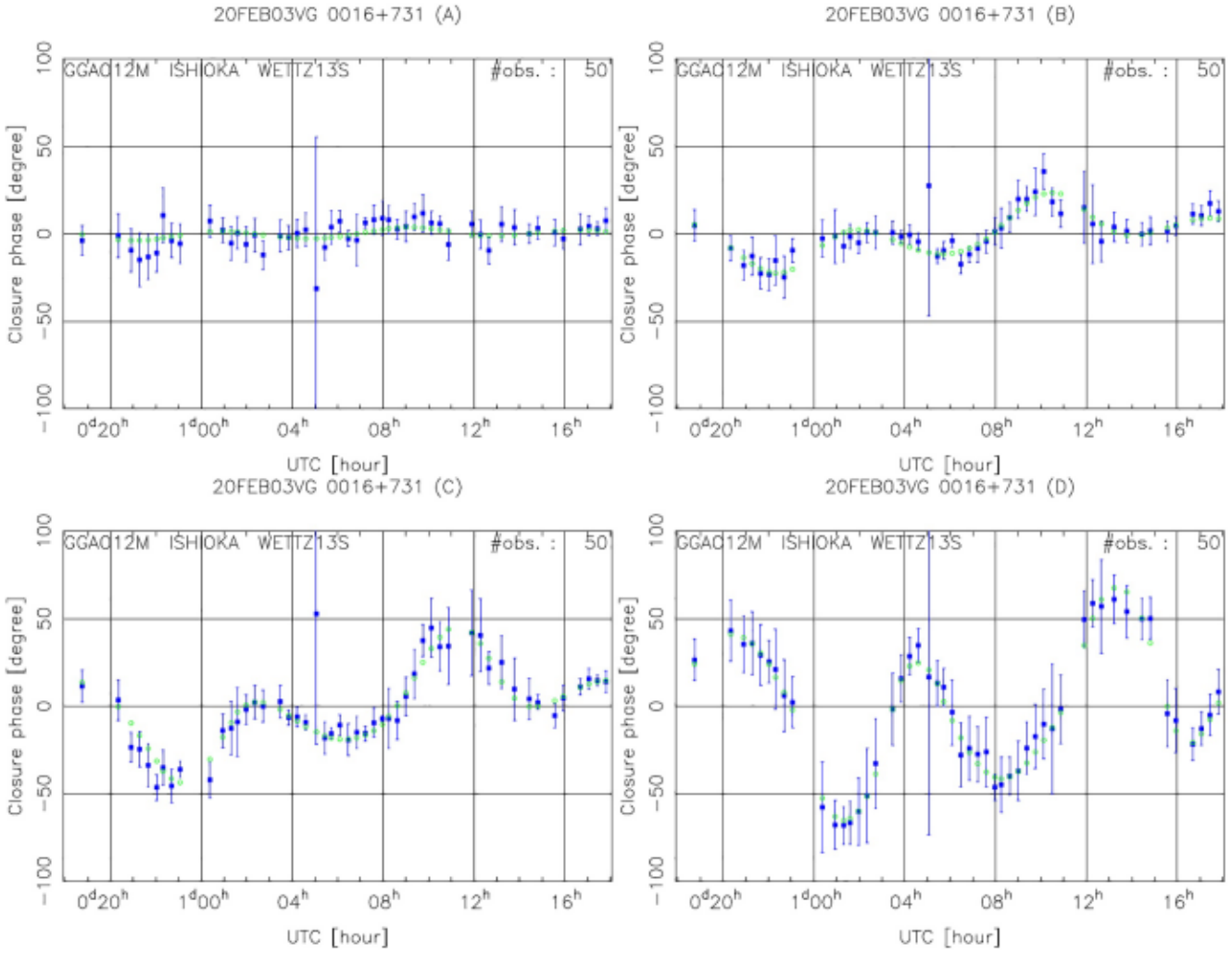

Figure A1. Observed closure phases (blue dots) and modeled closure phases (green open circles) of triangle GGAO12M-ISHIOKA-WETTZ13S for source 0016 + 731 at the frequencies 3.3 GHz (upper-left), 5.5 GHz (upper-right), 6.6 GHz (bottom-left), and 10.5 GHz (bottom-right) in session VO0034. The RMS values of the closure phases of this triangle are 6.5°, 12.5°, 22.5°, and 36.9° at the four bands; after subtracting the modeled closure phases, the RMS values of the residual closure phases are 5.5°, 5.0°, 6.0°, and 6.2°. RMS, root-mean-square.

A3. Images for Some Representative Sources

The images for seven other sources for which structure effects have been discussed in the main body of the paper are presented in Figures A2 and A5–A10. Comparison plots for closure phases and log closure amplitudes are shown for only source 1803 + 784 in Figures A3 and A4 as an example.

A4. MOJAVE Images of Six Sources

The images of six sources from the MOJAVE project were used in the study for simulation and comparison (Figure A11).

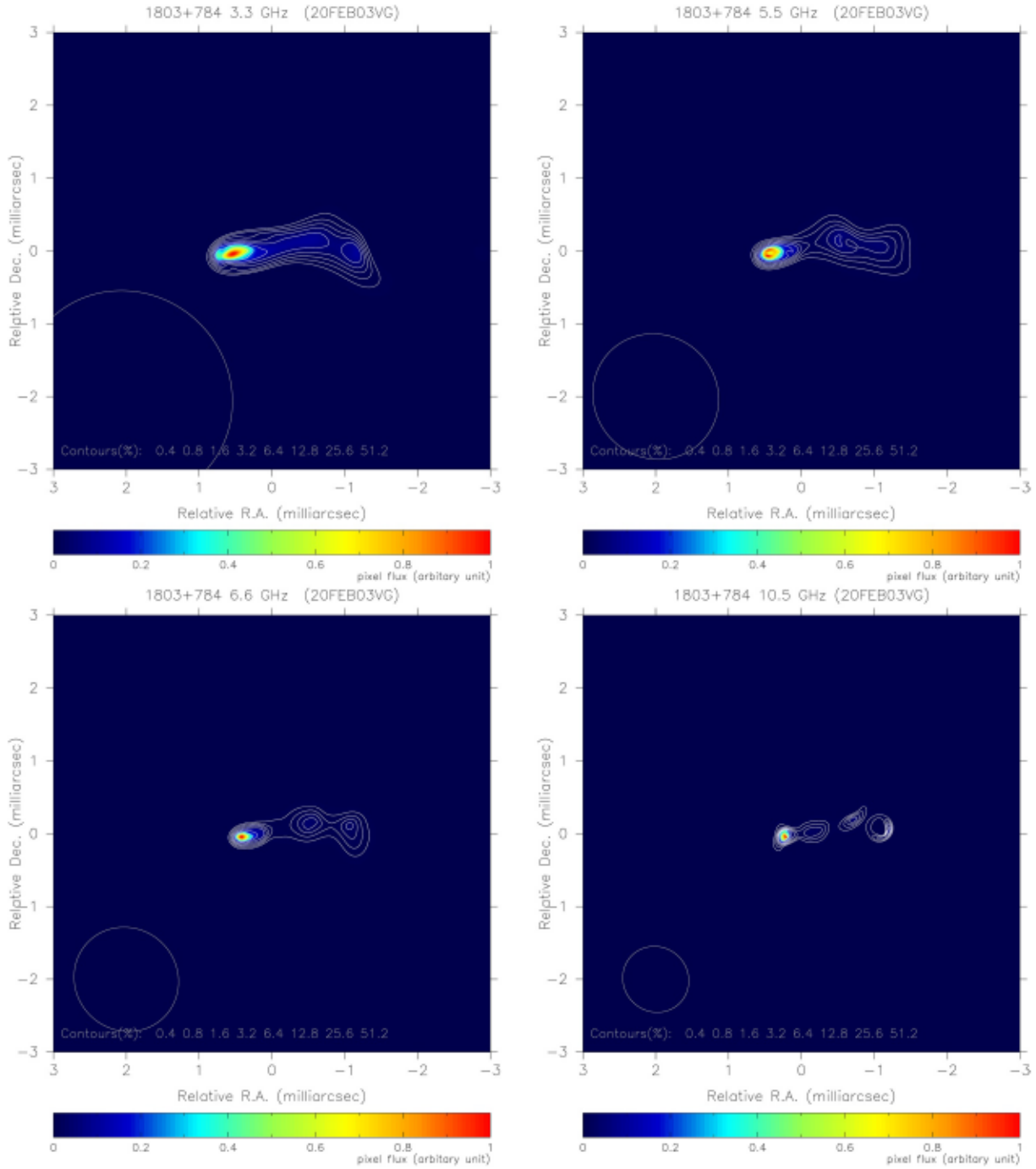

Figure A2. Images of source 1803 + 784 at the frequencies of 3.3, 5.5, 6.6, and 10.5 GHz from VGOS observations VO0034. Overlay contours are shown at eight levels of peak percentage (specified in the bottom of plots) in white. They were derived based on closure phases and closure amplitudes only. The mean positions are chosen as the reference points for the plots and the pixel fluxes are in arbitrary units. The coordinates of the peak flux are (0.543, −0.042), (0.468, −0.077), (0.426, −0.047), and (0.213, −0.062) mas for the four bands, respectively. The nominal beam is displayed as a gray ellipse in the bottom-left corner of each plot. VGOS, VLBI Global Observing System.

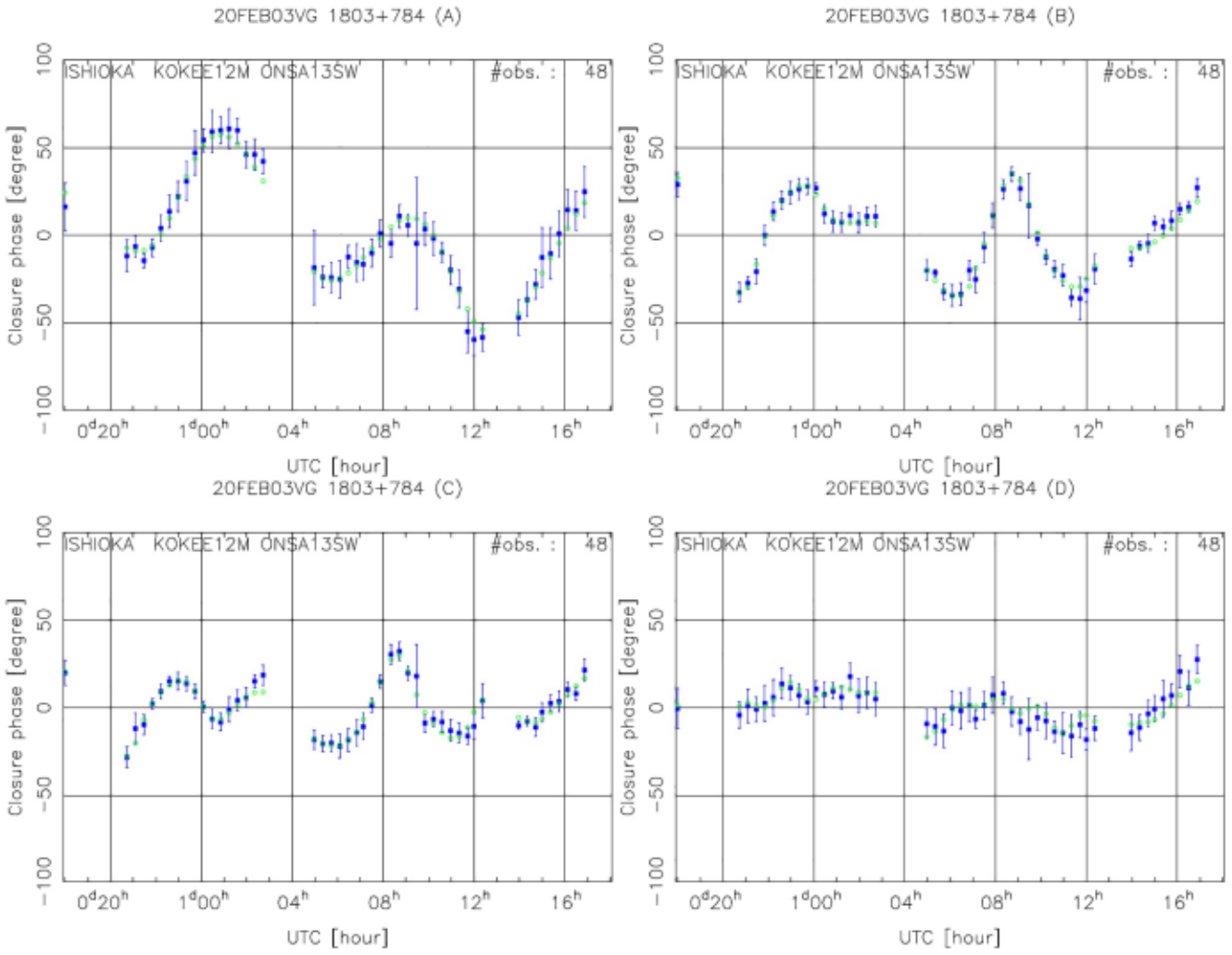

Figure A3. Observed closure phases (blue dots) and modeled closure phases (green open circles) of triangle ISHIOKA-KOKEE12M-ONSA13SW for source 1803 + 784 at the frequencies 3.3 GHz (upper-left), 5.5 GHz (upper-right), 6.6 GHz (bottom-left), and 10.5 GHz (bottom-right) in session VO0034.

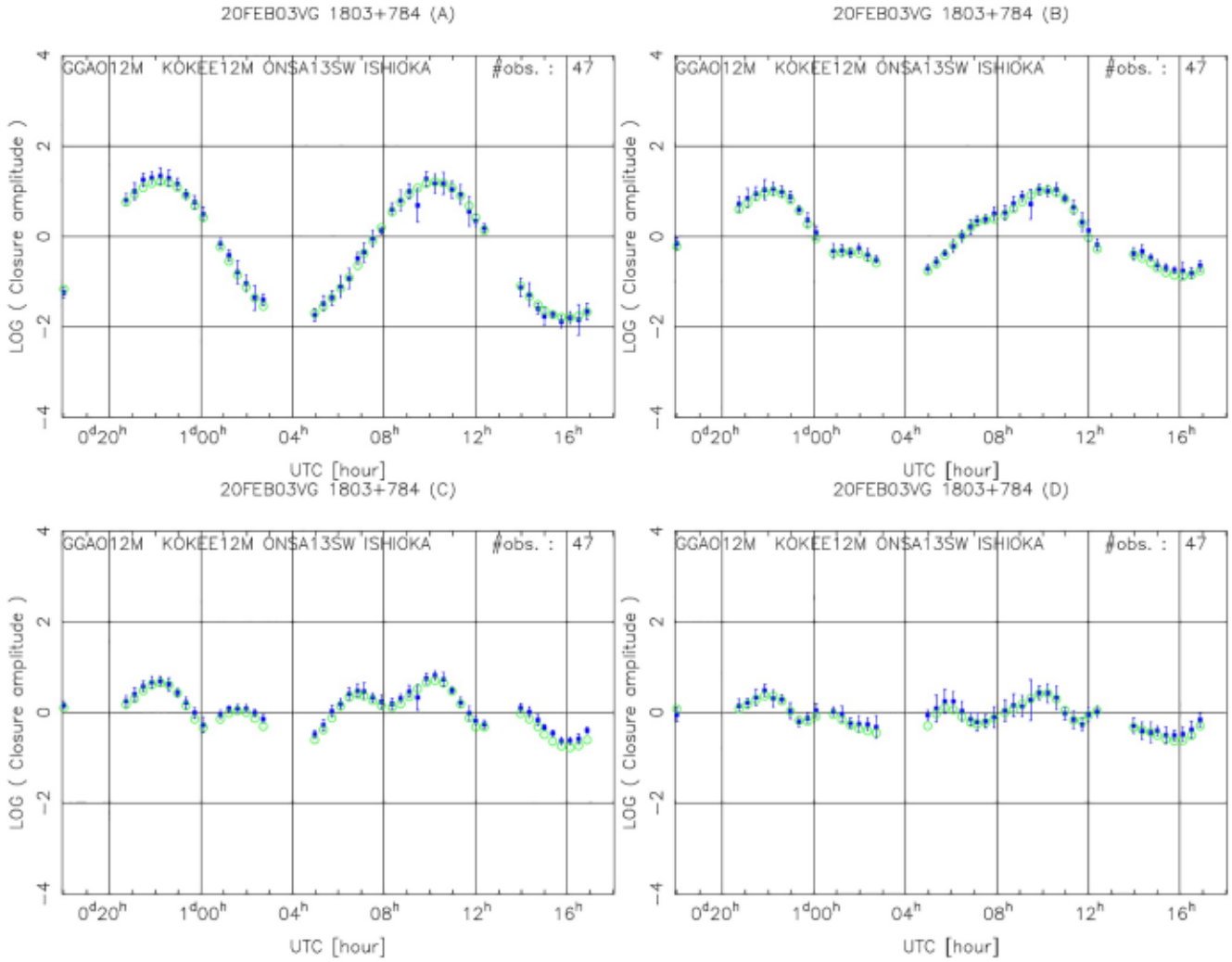

Figure A4. Observed log closure amplitudes (blue dots) and modeled log closure amplitudes (green open circles) of quadrangle GGAO12M-KOKEE12M-ONSA13SW-ISHIOKA for source 1803 + 784 at the frequencies 3.3 GHz (upper-left), 5.5 GHz (upper-right), 6.6 GHz (bottom-left), and 10.5 GHz (bottom-right) in session VO0034.

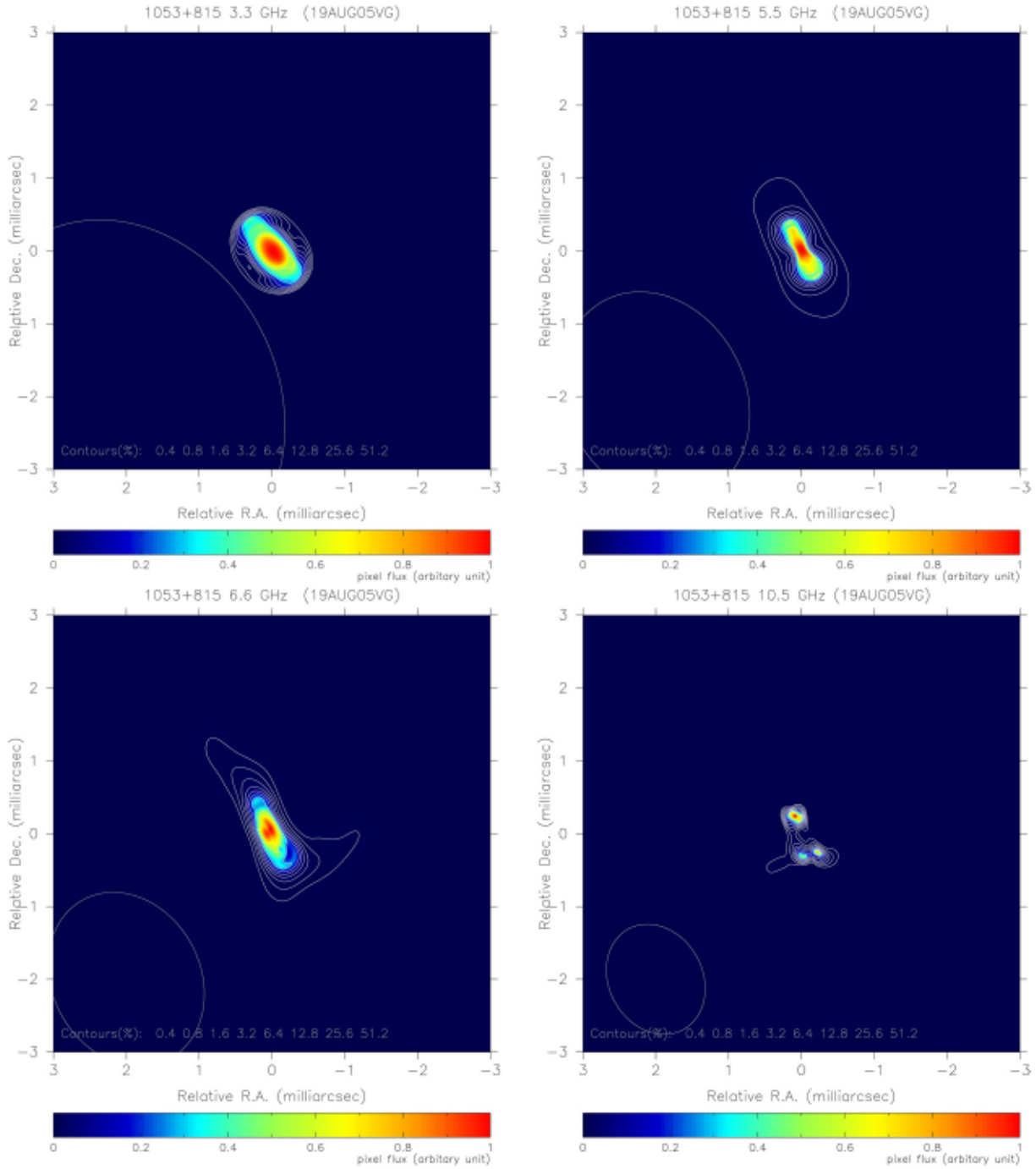

Figure A5. Images of source 1053 + 815 at the frequencies of 3.3, 5.5, 6.6, and 10.5 GHz from VGOS observations VT9217. Overlay contours are shown at eight levels of peak percentage (specified in the bottom of plots) in white. They were derived based on closure phases and closure amplitudes only. The mean positions are chosen as the reference points for the plots and the pixel fluxes are in arbitrary units. The coordinates of the peak flux are (−0.027, −0.016), (0.003, 0.008), (0.013, 0.056), and (0.082, 0.241) mas for the four bands, respectively. The nominal beam is displayed as a gray ellipse in the bottom-left corner of each plot. VGOS, VLBI Global Observing System.

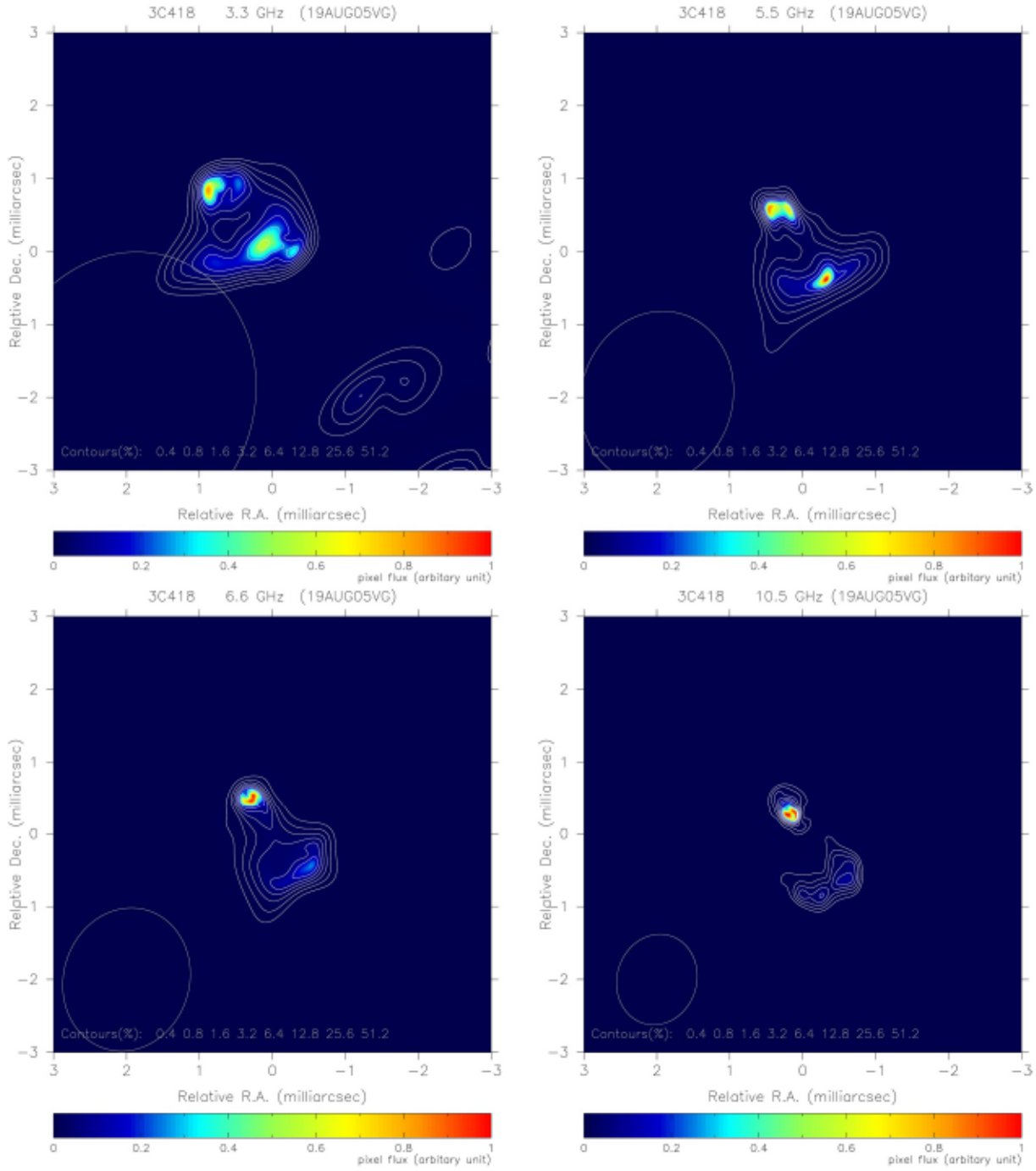

Figure A6. Images of source 3C418 at the frequencies of 3.3, 5.5, 6.6, and 10.5 GHz from VGOS observations VT9217. Overlay contours are shown at eight levels of peak percentage (specified in the bottom of plots) in white. They were derived based on closure phases and closure amplitudes only. The mean positions are chosen as the reference points for the plots and the pixel fluxes are in arbitrary units. The coordinates of the peak flux are (0.890, 0.832), (−0.318, −0.393), (0.258, 0.539), and (0.228, 0.259) mas for the four bands, respectively. The nominal beam is displayed as a gray ellipse in the bottom-left corner of each plot. VGOS, VLBI Global Observing System.

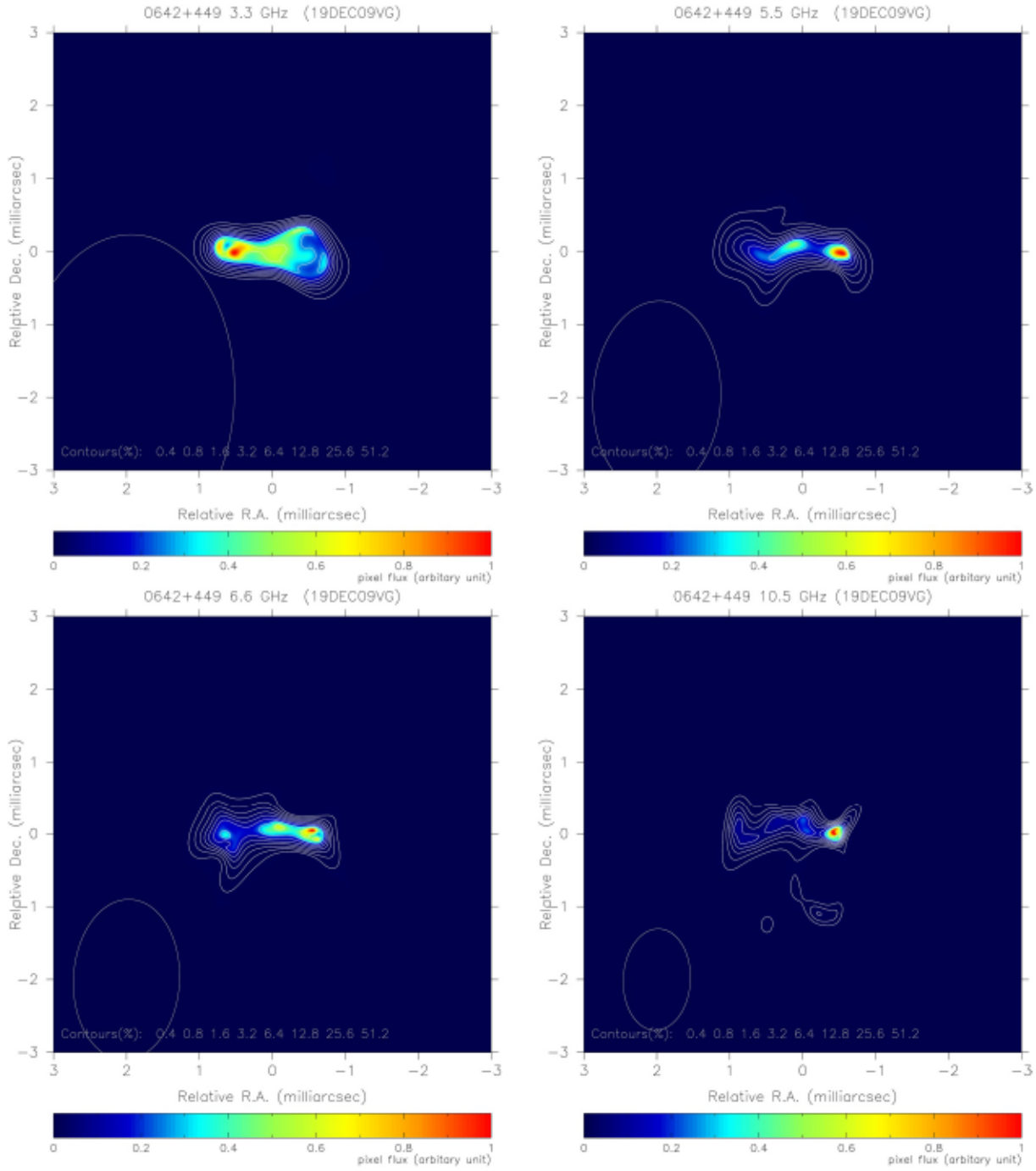

Figure A7. Images of source 0642 + 449 at the frequencies of 3.3, 5.5, 6.6, and 10.5 GHz from VGOS observations VT9343. Overlay contours are shown at eight levels of peak percentage (specified in the bottom of plots) in white. They were derived based on closure phases and closure amplitudes only. The mean positions are chosen as the reference points for the plots and the pixel fluxes are in arbitrary units. The coordinates of the peak flux are (0.533, −0.015), (−0.533, −0.028), (−0.547, 0.039), and (−0.407, 0.022) mas for the four bands, respectively. The nominal beam is displayed as a gray ellipse in the bottom-left corner of each plot. VGOS, VLBI Global Observing System.

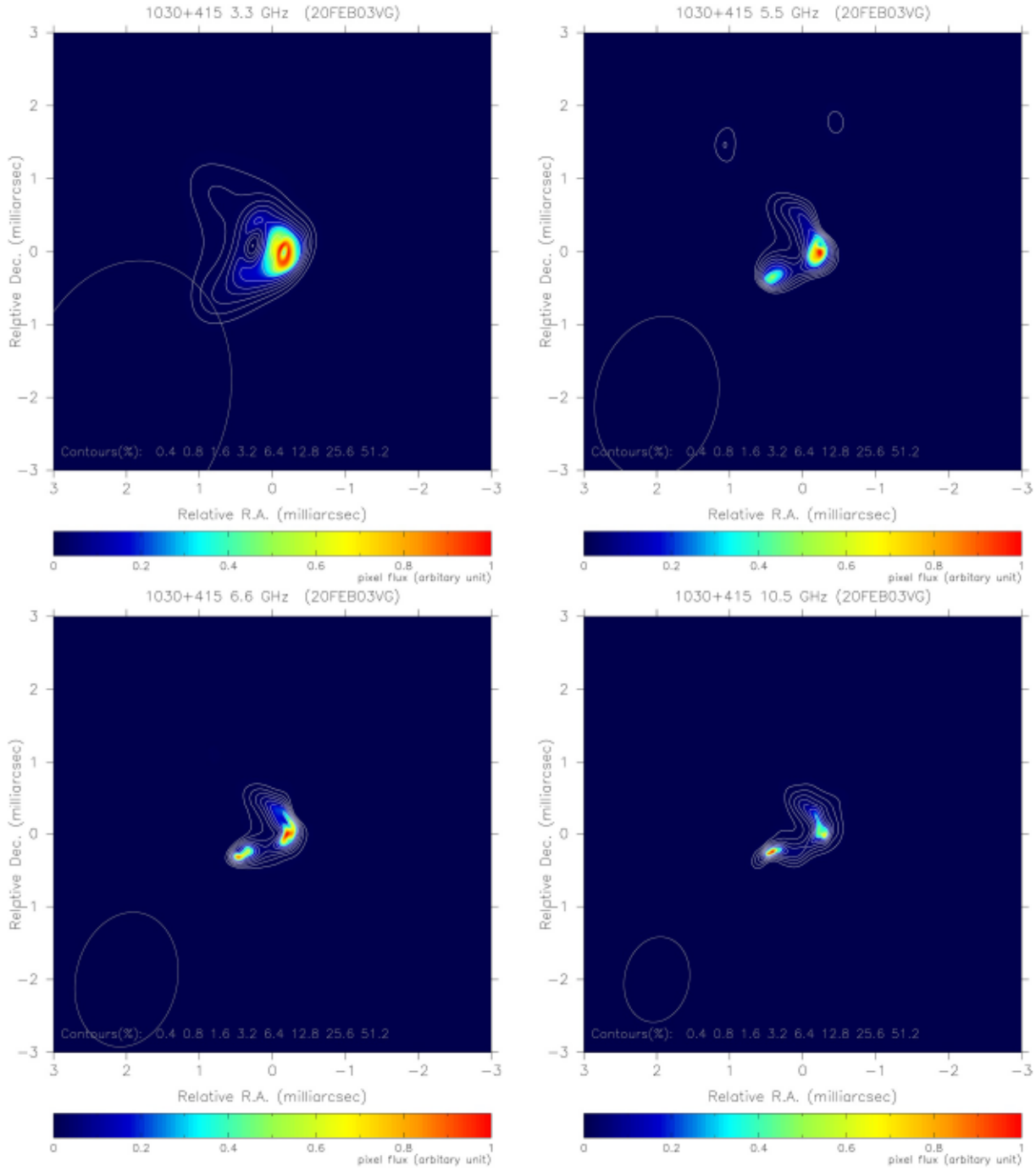

Figure A8. Images of source 1030 + 415 at the frequencies of 3.3, 5.5, 6.6, and 10.5 GHz from VGOS observations VO0034. Overlay contours are shown at eight levels of peak percentage (specified in the bottom of plots) in white. They were derived based on closure phases and closure amplitudes only. The mean positions are chosen as the reference points for the plots and the pixel fluxes are in arbitrary units. The coordinates of the peak flux are (−0.126, 0.042), (−0.233, −0.024), (−0.202, −0.011), and (0.420, −0.251) mas for the four bands, respectively. The nominal beam is displayed as a gray ellipse in the bottom-left corner of each plot. VGOS, VLBI Global Observing System.

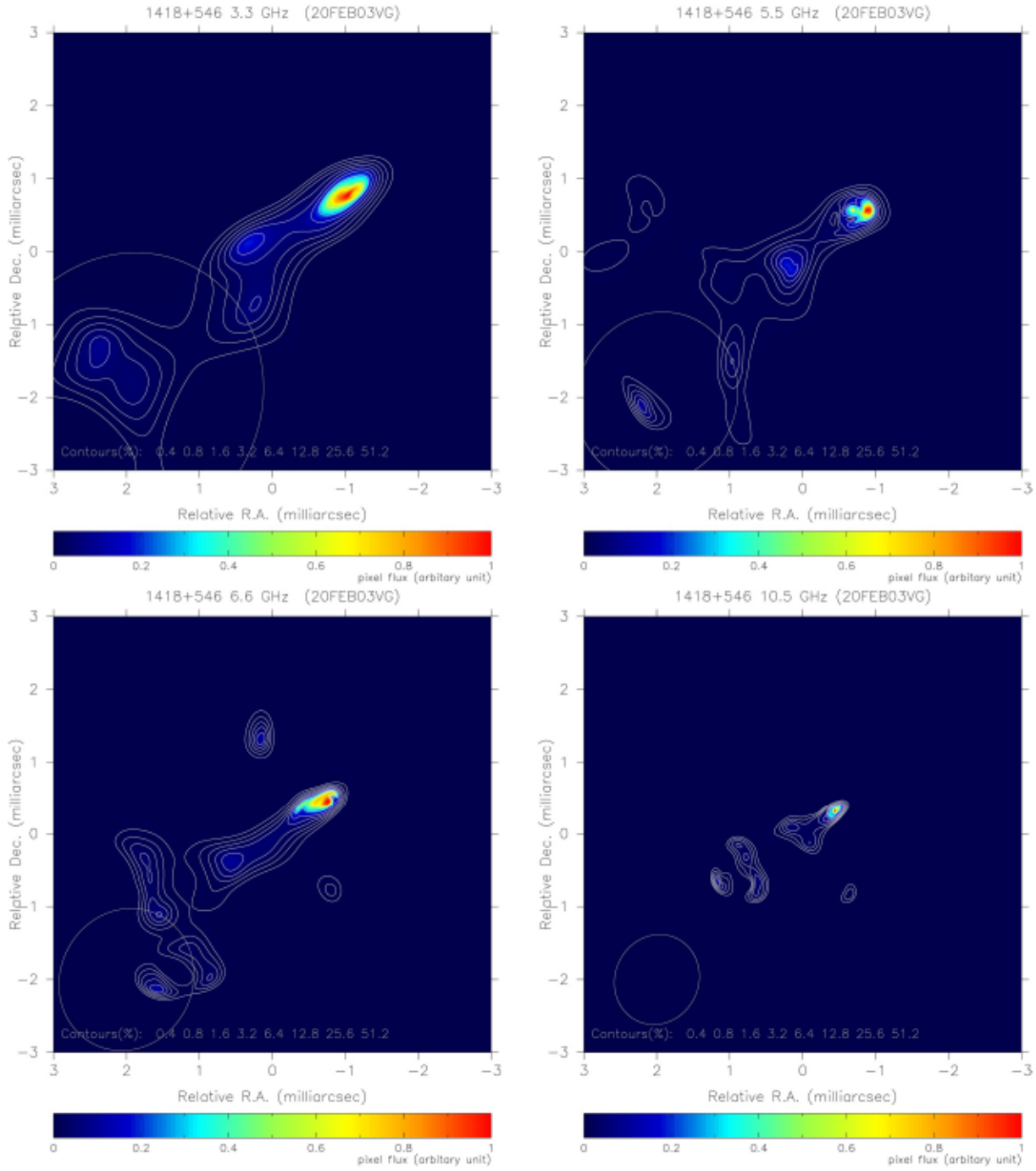

Figure A9. Images of source 1418 + 546 at the frequencies of 3.3, 5.5, 6.6, and 10.5 GHz from VGOS observations VO0034. Overlay contours are shown at eight levels of peak percentage (specified in the bottom of plots) in white. They were derived based on closure phases and closure amplitudes only. The mean positions are chosen as the reference points for the plots and the pixel fluxes are in arbitrary units. The coordinates of the peak flux are (−1.043, 0.780), (−0.873, 0.561), (−767, 0.448), and (−0.438, 0.320) mas for the four bands, respectively. The nominal beam is displayed as a gray ellipse in the bottom-left corner of each plot. VGOS, VLBI Global Observing System.

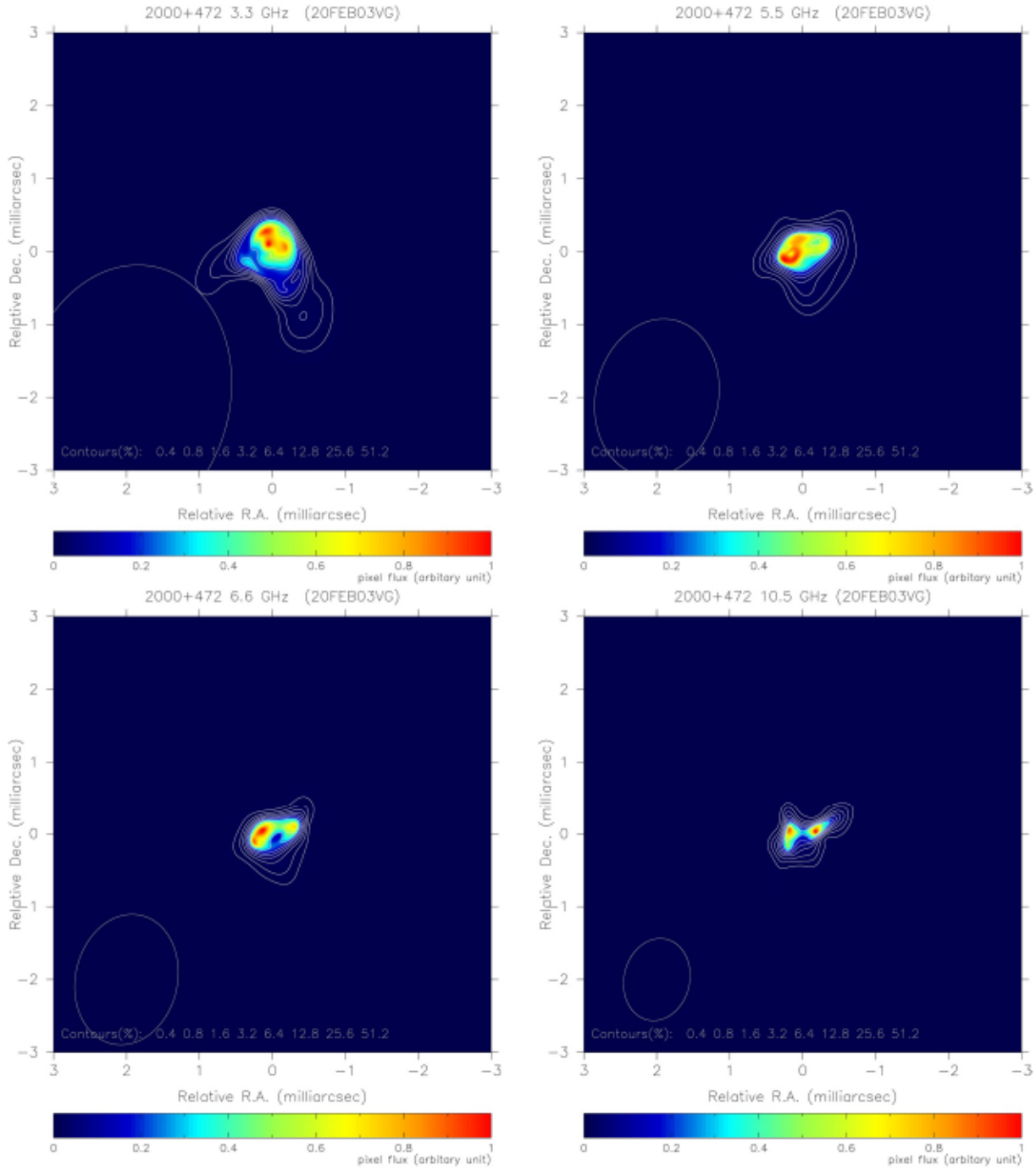

Figure A10. Images of source 2000 + 472 at the frequencies of 3.3, 5.5, 6.6, and 10.5 GHz from VGOS observations VO0034. Overlay contours are shown at eight levels of peak percentage (specified in the bottom of plots) in white. They were derived based on closure phases and closure amplitudes only. The mean positions are chosen as the reference points for the plots and the pixel fluxes are in arbitrary units. The coordinates of the peak flux are (0.056, 0.103), (0.252, −0.118), (0.134, 0.046), and (−0.167, 0.032) mas for the four bands, respectively. The nominal beam is displayed as a gray ellipse in the bottom-left corner of each plot. VGOS, VLBI Global Observing System.

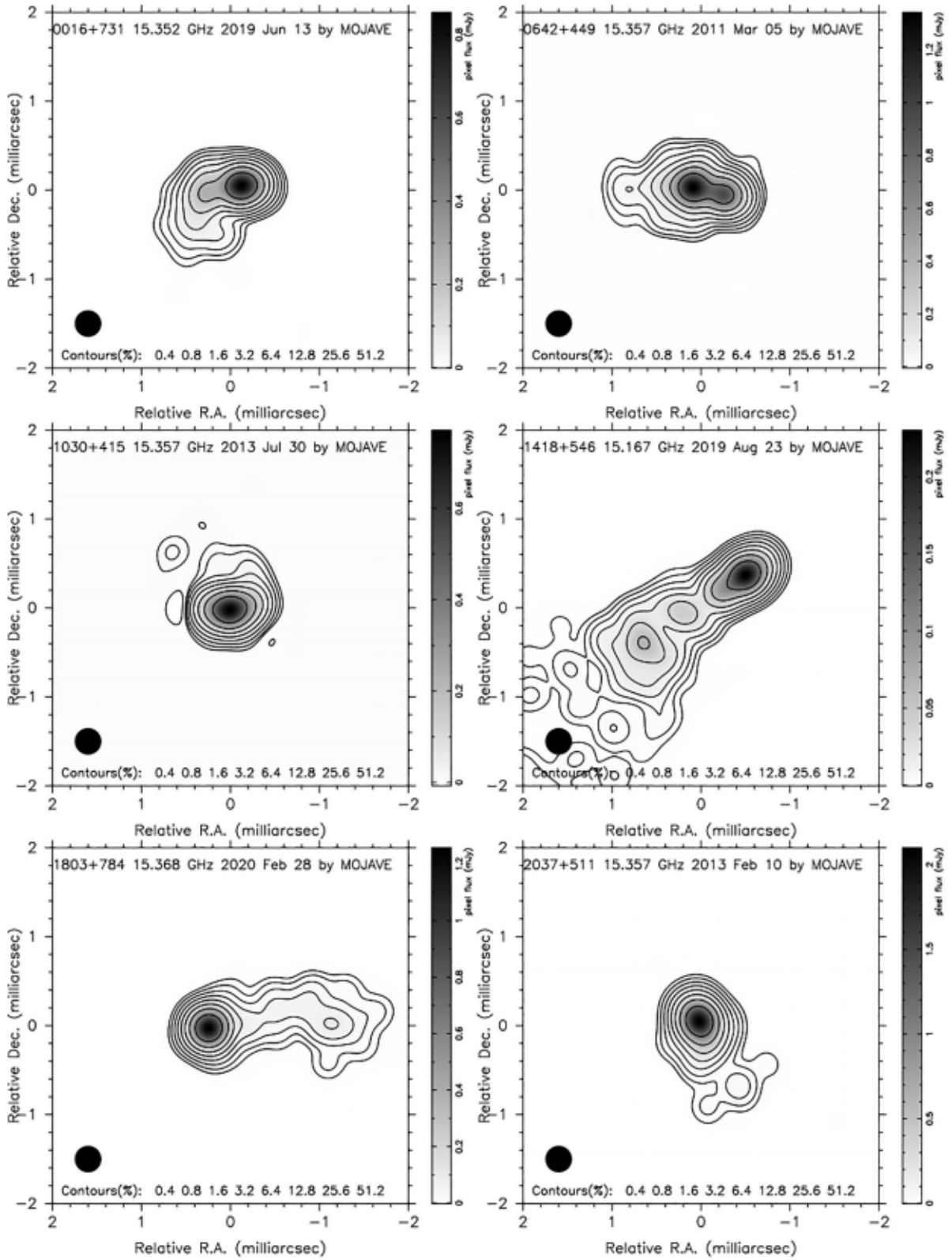

Figure A11. MOJAVE images of the six sources used for simulation and comparison at the epochs close to the VGOS observations. They were convolved with a circular beam of 0.3 mas, about 40% of the typical MOJAVE beam size. MOJAVE, Monitoring of Jets in Active galactic nuclei with VLBA Experiments; VGOS, VLBI Global Observing System.

Data Availability Statement

This research has made use of the Generic Mapping Tools package, the pgplot library, and the SAO/NASA Astrophysics Data System. This research has made use of data from the MOJAVE database that is maintained by the MOJAVE team (Lister et al., 2018). This research was supported by the Academy of Finland project No. 315721. Susanne Lunz is supported by the DFG Grant No. HE5937/2-2.

Acknowledgments
We would like to thank the two reviewers Sergei Bolotin and Arthur Niell for their helpful comments. The results reported in this study used the data owned by the International VLBI Service (IVS) and its international self-funded member organizations. We are grateful to the IVS VGOS stations at GGAO (MIT Haystack Observatory and NASA GSFC, USA), Ishioka (Geospatial Information Authority of Japan), Kokee Park (U.S. Naval Observatory and NASA GSFC, USA), McDonald (McDonald Geodetic Observatory and NASA GSFC, USA), Onsala (Onsala Space Observatory, Chalmers University of Technology, Sweden), Westford (MIT Haystack Observatory), Wettzell (Bundesamt für Kartographie und Geodäsie and Technische Universität München, Germany), and Yebes (Instituto Geográfico Nacional, Spain), to the staff at the MPIfR/BKG correlator center and the MIT Haystack Observatory correlator for performing the correlations and the fringe fitting of the data, to the NASA GSFC VLBI group for doing the geodetic solutions, and to the IVS Data Centers at BKG (Leipzig, Germany), Observatoire de Paris (France), and NASA CDDIS (Greenbelt, MD, USA) for the central data holds.

References

Akiyama, K., Kuramochi, K., Ikeda, S., Fish, V. L., Tazaki, F., Honma, M., et al. (2017). Imaging the Schwarzschild-radius-scale structure of M87 with the event horizon telescope using sparse modeling. *The Astrophysical Journal*, *838*(1), 1. https://doi.org/10.3847/1538-4357/aa6305

Altamimi, Z., Rebischung, P., Métivier, L., & Collilieux, X. (2016). ITRF2014: A new release of the International Terrestrial Reference Frame modeling nonlinear station motions. *Journal of Geophysical Research: Solid Earth*, *121*, 6109–6131. https://doi.org/10.1002/2016JB013098

Anderson, J. M., & Xu, M. H. (2018). Source structure and measurement noise are as important as all other residual sources in geodetic VLBI combined. *Journal of Geophysical Research: Solid Earth*, *123*, 10162–10190. https://doi.org/10.1029/2018JB015550

Blackburn, L., Pesce, D. W., Johnson, M. D., Wielgus, M., Chael, A. A., Christian, P., & Doeleman, S. S. (2020). Closure statistics in interferometric data. *The Astrophysical Journal*, *894*(1), 31. https://doi.org/10.3847/1538-4357/ab8469

Blandford, R. D., & Königl, A. (1979). Relativistic jets as compact radio sources. *The Astrophysical Journal*, *232*, 34–48. https://doi.org/10.1086/157262

Bolotin, S., Baver, K., Bolotina, O., Gipson, J., Gordon, D., Le Bail, K., & MacMillan, D. (2019). The source structure effect in broadband observations. In R. Haas, S. Garcia-Espada, & J. A. López Fernández (Eds.), *Proceedings of the 24th European VLBI group for geodesy and astrometry working meeting* (pp. 224–228). Madrid, Spain: Centro Nacional de Información Geográfica. Retrieved from https://space-geodesy.nasa.gov/docs/2019/SourceStructureEffectBroadbandObservations.pdf

Byrd, R. H., Lu, P., Nocedal, J., & Zhu, C. (1995). A limited memory algorithm for bound constrained optimization. *SIAM Journal on Scientific Computing*, *16*(5), 1190–1208. https://doi.org/10.1137/0916069

Cappallo, R. (2014). Correlating and fringe-fitting broadband VGOS data. In *International VLBI service for geodesy and astrometry 2014 general meeting proceedings: VGOS: The new VLBI network* (pp. 91–96). Retrieved from https://lvscc.gsfc.nasa.gov/publications/gm2014/019_Cappallo.pdf

Cappallo, R. (2015). Covariance analysis of the simultaneous fit of group delay and dTEC in fourfit. In *Documentation of HOPS* (pp. 1–5). Retrieved from https://www.haystack.mit.edu/tech/vlbi/hops/simul_ion_fit.pdf

Cappallo, R. (2016). Delay and phase calibration in VGOS post-processing. In *New horizons with VGOS* (pp. 61–64). Retrieved from https://lvscc.gsfc.nasa.gov/publications/gm2016/010_cappallo.pdf

Chael, A. A., Johnson, M. D., Bouman, K. L., Blackburn, L. L., Akiyama, K., & Narayan, R. (2018). Interferometric imaging directly with closure phases and closure amplitudes. *The Astrophysical Journal*, *857*(1), 23. https://doi.org/10.3847/1538-4357/aab6a8

Chael, A. A., Johnson, M. D., Narayan, R., Doeleman, S. S., Wardle, J. F. C., & Bouman, K. L. (2016). High-resolution linear polarimetric imaging for the event horizon telescope. *The Astrophysical Journal*, *829*(1), 11. https://doi.org/10.3847/0004-637X/829/1/11

Clark, B. G. (1980). An efficient implementation of the algorithm 'CLEAN'. *Astronomy and Astrophysics*, *89*(3), 377.

Cornwell, T. J., & Wilkinson, P. N. (1981). A new method for making maps with unstable radio interferometers. *Monthly Notices of the Royal Astronomical Society*, *196*, 1067–1086. https://doi.org/10.1093/mnras/196.4.1067

Dodson, R., Rioja, M. J., Molina, S. N., & Gómez, J. L. (2017). High-precision astrometric millimeter very long baseline interferometry using a new method for multi-frequency calibration. *The Astrophysical Journal*, *834*(2), 177. https://doi.org/10.3847/1538-4357/834/2/177

Event Horizon Telescope Collaboration, Akiyama, K., Alberdi, A., Alef, W., Asada, K., Azulay, R., et al. (2019). First M87 event horizon telescope results. IV. Imaging the central supermassive black hole. *The Astrophysical Journal Letters*, *875*(1), L4. https://doi.org/10.3847/2041-8213/ab0e85

Fey, A. L., Gordon, D., Jacobs, C. S., Ma, C., Gaume, R. A., Arias, E. F., et al. (2015). The second realization of the international celestial reference frame by very long baseline interferometry. The *Astronomical Journal*, *150*(2), 58. https://doi.org/10.1088/0004-6256/150/2/58

Gipson, J. (2012). IVS working group 4: VLBI data structures. In D. Behrend, & K. D. Baver (Eds.), *IVS 2012 general meeting proceedings, NASA/CP-2012-217504* (pp. 212–221). Greenbelt, MD: NASA Goddard Space Flight Center.

Hamaker, J. P., Bregman, J. D., & Sault, R. J. (1996). Understanding radio polarimetry. I: Mathematical foundations. *Astronomy and Astrophysics*, *117*, 137–147. https://doi.org/10.1051/aas:1996146

Högbom, J. A. (1974). Aperture synthesis with a non-regular distribution of interferometer baselines. *Astronomy and Astrophysics Supplement*, *15*, 417.

Kovalev, Y. Y., Lobanov, A. P., Pushkarev, A. B., & Zensus, J. A. (2008). Opacity in compact extragalactic radio sources and its effect on astrophysical and astrometric studies. *Astronomy & Astrophysics*, *483*, 759. https://doi.org/10.1051/0004-6361:20078679

Lister, M. L., Aller, M. F., Aller, H. D., Hodge, M. A., Homan, D. C., Kovalev, Y. Y., et al. (2018). MOJAVE. XV. VLBA 15 GHz Total Intensity and Polarization Maps of 437 Parsec-scale AGN Jets from 1996 to 2017. *The Astrophysical Journal Supplement*, *234*(1), 12. https://doi.org/10.3847/1538-4365/aa9c44

Lobanov, A. P. (1998). Ultracompact jets in active galactic nuclei. *Astronomy & Astrophysics*, *330*, 79–89.

Martí-Vidal, I., Marcaide, J. M., Alberdi, A., Pérez-Torres, M. A., Ros, E., & Guirado, J. C. (2011). Detection of jet precession in the active nucleus of M 81. *Astronomy & Astrophysics*, *533*, A111. https://doi.org/10.1051/0004-6361/201117211

Narayan, R., & Nityananda, R. (1986). Maximum entropy image restoration in astronomy. *Annual Review of Astronomy and Astrophysics*, *24*, 127–170. https://doi.org/10.1146/annurev.aa.24.090186.001015

Niell, A., Barrett, J., Burns, A., Cappallo, R., Corey, B., Derome, M., et al. (2018). Demonstration of a broadband very long baseline interferometer system: A new instrument for high-precision space geodesy. *Radio Science*, *53*(10), 1269–1291. https://doi.org/10.1029/2018RS006617

Niell, A., Whitney, A., Petrachenko, W., Schlüter, W., Vandenberg, N., Hase, H., et al. (2007). VLBI2010: A vision for future geodetic VLBI. In P. Tregoning & C. Rizos (Eds.), *Dynamic planet—Monitoring and understanding a dynamic planet with geodetic and oceanographic tools, edited by Paul tregoning and chris rizos* (p. 757). Berlin: Springer. Retrieved from https://link.springer.com/chapter/10.1007/978-3-540-49350-1_108

Nityananda, R., & Narayan, R. (1983). Reconstruction of a polarized brightness distribution by the maximum entropy method. *Astronomy and Astrophysics*, *118*(1), 194–196.

Nothnagel, A., Artz, T., Behrend, D., & Malkin, Z. (2017). International VLBI Service for Geodesy and Astrometry. Delivering high-quality products and embarking on observations of the next generation. *Journal of Geodesy*, *91*(7), 711–721. https://doi.org/10.1007/s00190-016-0950-5

Pearson, T. J., & Readhead, A. C. S. (1984). Image formation by self-calibration in radio astronomy. *Annual Review of Astronomy and Astrophysics*, *22*, 97–130. https://doi.org/10.1146/annurev.aa.22.090184.000525

Petrachenko, B., Niell, A., Behrend, D., Corey, B., Boehm, J., Charlot, P., et al. (2009). *Design Aspects of the VLBI2010 system*. Progress Report of the IVS VLBI2010 Committee. (Tech. Rep.). Retrieved from https://ivscc.gsfc.nasa.gov/publications/misc/TM-2009-214180.pdf

Plavin, A. V., Kovalev, Y. Y., Pushkarev, A. B., & Lobanov, A. P. (2019). Significant core shift variability in parsec-scale jets of active galactic nuclei. *Monthly Notices of the Royal Astronomical Society*, *485*(2), 1822–1842. https://doi.org/10.1093/mnras/stz504

Porcas, R. W. (2009). Radio astrometry with chromatic AGN core positions. *Astronomy & Astrophysics*, *505*(1), L1–L4. https://doi.org/10.1051/0004-6361/200912846

Porcas, R. W. (2010). VLBI2010: The Astro-geo connection. In *Sixth international VLBI service for geodesy and astronomy. Proceedings from the 2010 general meeting* (pp. 8–17). Retrieved from https://ivscc.gsfc.nasa.gov/publications/gm2010/porcas.pdf

Pushkarev, A. B., Hovatta, T., Kovalev, Y. Y., Lister, M. L., Lobanov, A. P., Savolainen, T., & Zensus, J. A. (2012). MOJAVE: Monitoring of Jets in Active galactic nuclei with VLBA Experiments. IX. Nuclear opacity. *Astronomy & Astrophysics*, *545*, A113. https://doi.org/10.1051/0004-6361/201219173

Reid, M. J., & Honma, M. (2014). Microarcsecond radio astrometry. *Annual Review of Astronomy and Astrophysics*, *52*, 339–372. https://doi.org/10.1146/annurev-astro-081913-040006

Rioja, M. J., Dodson, R., Jung, T., & Sohn, B. W. (2015). The power of simultaneous multifrequency observations for mm-VLBI: Astrometry up to 130 GHz with the KVN. The *Astronomical Journal*, *150*(6), 202. https://doi.org/10.1088/0004-6256/150/6/202

Ros, E., Marcaide, J. M., Guirado, J. C., & Pérez-Torres, M. A. (2001). Absolute kinematics of radio source components in the complete S5 polar cap sample. I. First and second epoch maps at 8.4 GHz. *Astronomy & Astrophysics*, *376*, 1090–1105. https://doi.org/10.1051/0004-6361:20010987

Schuh, H., & Behrend, D. (2012). VLBI: A fascinating technique for geodesy and astrometry. *Journal of Geodynamics*, *61*, 68–80. https://doi.org/10.1016/j.jog.2012.07.007

Sokolovsky, K. V., Kovalev, Y. Y., Pushkarev, A. B., & Lobanov, A. P. (2011). A VLBA survey of the core shift effect in AGN jets. I. Evidence of dominating synchrotron opacity. *Astronomy & Astrophysics*, *532*, A38. https://doi.org/10.1051/0004-6361/201016072

Thompson, A. R., Moran, J. M., Swenson, J., & George, W. (2017). *Interferometry and synthesis in radio astronomy* (3rd ed.). New York: Springer. https://doi.org/10.1007/978-3-319-44431-4

Wilkinson, P. N., Readhead, A. C. S., Purcell, G. H., & Anderson, B. (1977). Radio structure of 3C 147 determined by multi-element very long baseline interferometry. *Nature*, *269*, 764–768. https://doi.org/10.1038/269764a0

Xu, M. H., Anderson, J. M., Heinkelmann, R., Lunz, S., Schuh, H., & Wang, G. L. (2019). Structure effects for 3417 celestial reference frame radio sources. *The Astrophysical Journal—Supplement Series*, *242*(1), 5. https://doi.org/10.3847/1538-4365/ab16ea

Xu, M. H., Anderson, J. M., Heinkelmann, R., Lunz, S., Schuh, H., & Wang, G. L. (2020). Observable quality assessment of broadband very long baseline interferometry system. *Journal of Geodesy*. arXiv:2102.12750. https://doi.org/10.1007/s00190-021-01496-7

Xu, M. H., Heinkelmann, R., Anderson, J. M., Mora-Diaz, J., Karbon, M., Schuh, H., & Wang, G. L. (2017). The impacts of source structure on geodetic parameters demonstrated by the radio source 3C371. *Journal of Geodesy*, *91*(7), 767–781. https://doi.org/10.1007/s00190-016-0990-x

Xu, M. H., Heinkelmann, R., Anderson, J. M., Mora-Diaz, J., Schuh, H., & Wang, G. L. (2016). The source structure of 0642+449 detected from the CONT14 observations. The *Astronomical Journal*, *152*(5), 151. https://doi.org/10.3847/0004-6256/152/5/151

Xu, M. H., Lunz, S., Anderson, J. M., Savolainen, T., Zubko, N., Schuh, H. (2021). Evidence of the Gaia–VLBI position differences being related to radio source structure. *Astronomy & Astrophysics*, *647*, A189. http://dx.doi.org/10.1051/0004-6361/202040168